Stepwise gating of the Sec61 protein-conducting channel by Sec63 and Sec62

Samuel Itskanov [1], Katie M. Kuo[2], James C. Gumbart[2,3] and Eunyong Park [4,5] ✉

Many proteins are transported into the endoplasmic reticulum by the universally conserved Sec61 channel. Post-translational transport requires two additional proteins, Sec62 and Sec63, but their functions are poorly defined. In the present study, we determined cryo-electron microscopy (cryo-EM) structures of several variants of Sec61–Sec62–Sec63 complexes from *Saccharomyces cerevisiae* and *Thermomyces lanuginosus* and show that Sec62 and Sec63 induce opening of the Sec61 channel. Without Sec62, the translocation pore of Sec61 remains closed by the plug domain, rendering the channel inactive. We further show that the lateral gate of Sec61 must first be partially opened by interactions between Sec61 and Sec63 in cytosolic and luminal domains, a simultaneous disruption of which completely closes the channel. The structures and molecular dynamics simulations suggest that Sec62 may also prevent lipids from invading the channel through the open lateral gate. Our study shows how Sec63 and Sec62 work together in a hierarchical manner to activate Sec61 for post-translational protein translocation.

In all organisms, about a third of proteins are transported across or integrated into a membrane upon synthesis by the ribosome. Most of these translocation processes occur in the endoplasmic reticulum (ER) membrane in eukaryotes or the plasma membrane in prokaryotes, mediated by the conserved, heterotrimeric, protein-conducting channel called the Sec61 (SecY in prokaryotes) complex[1-5]. The main (α) subunit of the channel, comprising ten transmembrane helices (TMs), forms an hourglass-shaped cavity, through which polypeptides are transported as extended chains. The small β and γ subunits peripherally associate with the α subunit in the membrane[6]. Previous structures of Sec61 and SecY showed that in the idle state the pore is blocked in the ER luminal (or extracellular) funnel by the plug domain—a structure formed by a segment immediately after TM1 of the α subunit[6-9], whereas in translocating states the plug moves away[10-12]. The channel can also release polypeptides to the lipid phase through a gap (lateral gate) formed between TM2 and TM7 of the α subunit. The opening of the lateral gate is required for recognition of hydrophobic targeting signals (signal sequences) of soluble secretory proteins and integration of transmembrane proteins. Thus, the channel is gated in two directions: vertically across the membrane by the plug domain and laterally within the membrane by the lateral gate. How these gates are controlled and how they regulate the translocation processes remain incompletely understood.

The Sec61 (or SecY) channel alone is inactive and thus must associate with a partner to enable translocation. In the co-translational mode, common in both prokaryotes and eukaryotes, the channel directly docks with the ribosome–nascent chain complex[11,13,14]. Many secretory proteins are targeted to the channel post-translationally after their release from the ribosome[15-20]. In bacteria, a single cytosolic ATPase called SecA binds to the SecY complex to drive post-translational translocation[10,12,19-21]. In eukaryotes, post-translational translocation is enabled by association between the Sec61 complex and the two essential integral membrane proteins Sec62 and Sec63, forming the so-called Sec complex[22-25]. In fungal species, the Sec complex also contains the additional nonessential proteins Sec71 and Sec72, which are bound to Sec63 in the cytosol. In the ER lumen, Sec63 recruits the heat-specific protein Hsp70 ATPase BiP to the complex to power translocation[26,27].

Recently, two cryo-EM studies reported structures of the Sec complex from *S. cerevisiae* at ~4-Å resolution[28,29], which suggested a putative role of Sec63 in activating the Sec61 channel for translocation by opening the lateral gate of the channel. However, in both structures, Sec62 was barely visible and thus its function remains unknown despite its essentiality. Furthermore, the two structures displayed noticeable conformational differences in Sec61, despite essentially identical specimen compositions. Most notably, in one structure the pore is blocked by the plug domain[29], whereas in the other structure the plug is displaced leaving the pore open[28]. Although deemed to be important given the role of the plug domain in channel gating, the cause of this difference remains a puzzle. Finally, although it has been suggested that Sec63 opens the lateral gate of Sec61 (refs. [28,29]), the mechanism of opening remains speculative without structures of mutants and other conformations. Thus, whether and how Sec62 and Sec63 regulate the function of Sec61 are poorly understood. Addressing these issues is essential for our understanding of eukaryotic post-translational translocation and the mechanism of the Sec61 and SecY channels in general.

In the present study, using cryo-EM, we analyzed several variants and mutants of the Sec complex from two fungal species, *S. cerevisiae* and *T. lanuginosus*. We show that Sec62 and Sec63 cooperate to open both the lateral and the vertical gates of the Sec61 channel. The structures and molecular dynamics (MD) simulations also suggest that Sec62 performs an additional function of preventing lipids from invading the channel through the open lateral gate. Our study provides a detailed mechanistic model for how Sec62 and Sec63 activate the Sec61 channel for post-translational protein translocation in eukaryotes.

¹Biophysics Graduate Program, University of California, Berkeley, CA, USA. ²School of Chemistry and Biochemistry, Georgia Institute of Technology, Atlanta, GA, USA. ³School of Physics, Georgia Institute of Technology, Atlanta, GA, USA. ⁴Department of Molecular and Cell Biology, University of California, Berkeley, CA, USA. ⁵California Institute for Quantitative Biosciences, University of California, Berkeley, CA, USA.
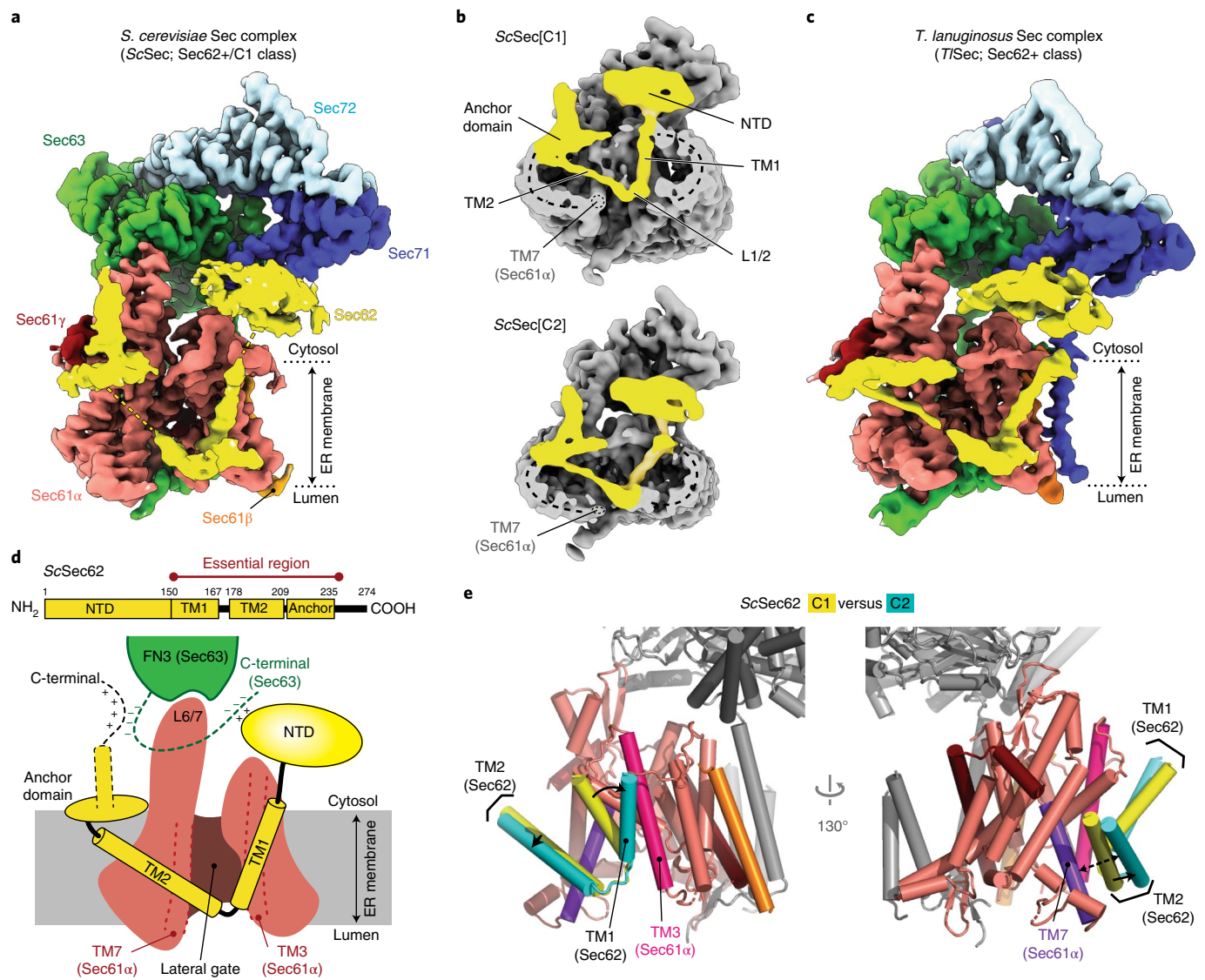✉e-mail: eunyong_park@berkeley.edu

Fig. 1 | Cryo-EM analysis of fungal Sec complexes and the structure of Sec62. a, The 3.1-Å-resolution cryo-EM reconstruction of the *Sc*Sec complex (C1 class, front view into the lateral gate). Yellow dashed lines indicate the connections that are visible at a lower contour level (see **b**). In yeast nomenclature, the α, β and γ subunits of the Sec61 complex are called Sec61p, Sbh1p and Sss1p, respectively. **b**, Cutaway views showing Sec62 (yellow). The 6-Å-low pass-filtered C1 (upper panel; a tilted view from the ER lumen) and C2 (lower panel; front view) maps are shown. The dashed line is a detergent micelle. **c**, The 3.8-Å-resolution reconstruction of the *T. lanuginosus* Sec complex (the consensus Sec62+ map). **d**, Domain organization of Sec62. Previous studies suggest an interaction between the NTD of Sec62 and the C-terminal tail of Sec63 (refs. [30,43]). In addition, based on proximity, the C-terminal tails of Sec62 and Sec63 may also interact with each other through an electrostatic interaction. **e**, Interactions between the Sec62 TMs and lateral gate. The dashed arrow is a gap between Sec61α-TM7 and Sec62-TM2 in the C2 conformation. Sec61α is colored salmon with TM3 and TM7 colored magenta and violet, respectively. Sec61β and Sec61γ are orange and dark red, respectively. Sec62 is in yellow (C1) or cyan (C2). Sec63, Sec71 and Sec72 are gray.

Results

Cryo-EM analysis of two fungal Sec complexes. To determine how the gating of the Sec61 channel is regulated in the Sec complex, we first analyzed a large cryo-EM dataset of the wild-type (WT) Sec complex from *S. cerevisiae* (*Sc*Sec) (Fig. 1a,b, Table 1 and Extended Data Fig. 1). Although reconstruction from approximately 1 million particles yielded a 3.0-Å-resolution consensus map (Extended Data Fig. 1b–d), we found that the particle set contained subpopulations lacking Sec62 or Sec71–Sec72, despite apparent sample homogeneity (Extended Data Fig. 1a). We therefore performed additional three-dimensional (3D) classifications to separate particles with and without Sec62 (referred to as Sec62+ and Sec62−; Extended Data Fig. 1b,e). Furthermore, the Sec62+ class could be further separated into two distinct subclasses (referred

to as C1 and C2), which show notable conformational differences in Sec62, the lateral gate and the plug (Fig. 1b and Extended Data Fig. 1f,g; see below). The three structures (that is, Sec62−, C1 and C2) were resolved at overall resolutions of 3.1–3.2 Å. Although an atomic model for Sec62 could not be built due to insufficient local resolution, the classification substantially improved Sec62 features, enabling unambiguous assignment of individual domains (Fig. 1a,d).

To gain insights into structural and mechanistic conservation across species, we also purified the Sec complex from the thermophilic fungus *T. lanuginosus* (*Tl*Sec) and determined its structures at overall resolutions of 3.6–3.9 Å (Fig. 1c, Table 1 and Extended Data Fig. 2). Recombinant expression of the *Tl*Sec complex allowed us to analyze complexes completely lacking Sec62 (ΔSec62 *Tl*Sec) or

Table 1 | Cryo-EM data collection, refinement and validation statistics of WT *Sc*Sec and WT and mutant *Tl*Sec complexes

	*Sc*Sec[Sec62−] (EMD-22770, PDB 7KAH)	*Sc*Sec[C1] (EMD-22771, PDB 7KAI)	*Sc*Sec[C2] (EMD-22772, PDB 7KAJ)	*Tl*Sec[Sec62−] (EMD-22773, PDB 7KAK)	*Tl*Sec[plug-open] (EMD-22774, PDB 7KAL)	*Tl*Sec[plug-closed] (EMD-22775, PDB 7KAM)	ΔSec62 *Tl*Sec (EMD-22776, PDB 7KAN)	Δanchor *Tl*Sec (EMD-22777)
Data collection and processing								
Magnification	×64,000	×64,000	×64,000	×36,000	×36,000	×36,000	×36,000	×64,000
Voltage (kV)	300	300	300	200	200	200	200	300
Electron exposure (e−/Å²)	49.1	49.1	49.1	50.0	50.0	50.0	50.0	49.1
Defocus range (µm)	−0.8 to −2.5	−0.8 to −2.5	−0.8 to −2.5	−0.6 to −2.4	−0.6 to −2.4	−0.6 to −2.4	−0.9 to −2.2	−0.7 to −2.9
Pixel size (Å)	1.19	1.19	1.19	1.14	1.14	1.14	1.14	1.19
Symmetry imposed	C1	C1	C1	C1	C1	C1	C1	C1
Initial particle images (no.)	2,686,839	2,686,839	2,686,839	1,632,659	1,632,659	1,632,659	546,712	229,825
Final particle images (no.)	391,885	193,263	193,661	155,601	114,704	143,227	222,047	76,726
Map resolution (Å)	3.1	3.2	3.1	3.9	4.0	3.8	3.7	4.4
FSC threshold	0.143	0.143	0.143	0.143	0.143	0.143	0.143	0.143
Map resolution range (Å)	2.6–11	2.8–12	2.7–12	3.4–13	3.3–13	3.3–12	3.3–12	3.7–14
Refinement								
Initial model used	PDB 6N3Q	PDB 7KAH	PDB 7KAH	PDB 7KAN	PDB 7KAN	PDB 7KAN	PDB 6N3Q	–
Model resolution (Å)	3.2	3.3	3.3	4.1	4.2	4.0	4.0	–
FSC threshold	0.5	0.5	0.5	0.5	0.5	0.5	0.5	–
Map sharpening B factor (Å²)	86.6	80.8	75.9	110.3	90.7	105.2	127.8	–
Model composition								
Nonhydrogen atoms	10,495	10,718	10,712	10,438	10,794	10,921	10,661	–
Protein residues	1,349	1,399	1,399	1,371	1,429	1,445	1,371	–
Ligands	–	–	–	–	–	–	2	–
B factors (Å²)								
Protein	73	61	58	117	126	74	30	–
Ligand	–	–	–	–	–	–	34	–
R.m.s. deviations								
Bond lengths (Å)	0.003	0.003	0.003	0.002	0.002	0.003	0.003	–
Bond angles (°)	0.522	0.508	0.513	0.524	0.489	0.521	0.623	–
Validation								
MolProbity score	1.43	1.42	1.33	1.51	1.42	1.48	1.55	–
Clashscore	4.61	4.14	3.87	6.33	5.62	5.60	6.18	–
Poor rotamers (%)	0	0	0	0	0	0	0	–
Ramachandran plot								
Favored (%)	96.83	96.58	97.01	97.09	97.42	96.96	96.72	–
Allowed (%)	3.17	3.42	2.99	2.91	2.58	3.04	3.28	–
Disallowed (%)	0	0	0	0	0	0	0	–

containing a mutant Sec62 copy for structural comparisons. Similar to WT *Sc*Sec, the WT *Tl*Sec dataset yielded two classes with and without Sec62 (referred to as *Tl*Sec[Sec62+] and *Tl*Sec[Sec62−]), which closely resemble the *Sc*Sec[C2] and [Sec62−] structures, respectively (brackets denote classes). We could not find a C1-equivalent class from the *Tl*Sec dataset, perhaps because the specimen freezing condition (4 °C) might have biased the conformation distribution of this thermophilic complex toward C2. The structure of *Tl*Sec[Sec62−] was found to be essentially identical to a separately determined structure of ΔSec62 *Tl*Sec, validating our approach to separate distinct subpopulations of the Sec complexes by cryo-EM image analysis (Extended Data Fig. 2g–i). Importantly, the domain arrangement of *Tl*Sec62 is the same as that of *Sc*Sec62

despite ~30% overall sequence identity (Fig. 1c and Supplementary Fig. 1). This corroborates the conserved architecture of Sec62. Compared with *Sc*Sec62, *Tl*Sec62 is better resolved such that we could register amino acids to its TM1.

Sec62 forms a V-shaped structure. Sec62 consists of a cytosolic, globular, N-terminal domain (NTD), two TMs (TM1 and TM2) connected by a short ER luminal loop (L1/2), and a cytosolic C-terminal segment (Fig. 1d). Functionally essential regions have previously been mapped to the two TMs and a segment of ~30 amino acids immediately after TM2 (ref. [30]). The TMs of Sec62 are arranged as a V shape in front of the lateral gate with L1/2 directed to the lateral gate opening (Fig. 1a–d). The contact with the channel

is mainly formed by an interaction of Sec62-TM1 with TM3 and the N-terminal segment of Sec61α.

After TM2, Sec62 contains an oval-shaped structure lying flat on the membrane interface (Fig. 1a–d and Extended Data Fig. 3a–c). This amphipathic structure, which we termed the anchor domain, is most probably formed by an ~20-residue-long conserved segment within the above-mentioned 30 amino acids, and is rich in hydrophobic amino acids (Supplementary Fig. 1). Although single-point mutations of these hydrophobic residues caused no growth defect, alanine substitutions of three consecutive residues in positions 215–220 were lethal (Extended Data Fig. 3d), suggesting that decreased hydrophobicity interrupts its functionally essential interaction with the membrane. The structure of a *Tl*Sec mutant (Δanchor *Tl*Sec) with the anchor domain replaced with a glycine/serine linker showed virtually no visible Sec62 features (Extended Data Fig. 3e,f), suggesting that Sec62 becomes too mobile without the domain. Taken together, these observations suggest that the function of the anchor domain is to properly position the V-shaped TMs of Sec62 at the lateral gate.

The revealed position and topology of Sec62 raise an important question about how the channel would engage with substrate polypeptides. During the initial stage of post-translational translocation, a substrate polypeptide is expected to insert into the channel as a loop with both its N- and C-termini exposed to the cytosol[31] (Extended Data Fig. 4a). Although the N-terminal signal sequence may sit initially at the lateral gate, as seen in structures of mammalian co-translational and bacterial post-translational complexes[10–12], later it must engage with the signal peptidase for cleavage[32]. Although the exact timing of the signal sequence cleavage remains unknown, the presence of Sec62 might pose a problem in this step because it may block the release of the signal sequence from the lateral gate or prevent the signal peptidase from accessing the cleavage site. The answer may be provided by a conformational transition from C1 to C2 as visualized in the *Sc*Sec structure (Fig. 1e). Although in both structures the seam between Sec62-TM1 and Sec61α-TM3 is tight, a sufficient gap is formed on the other side of the lateral gate between Sec62-TM2 and Sec61α-TM7 in the *Sc*Sec[C2] structure. A similar gap also exists in the *Tl*Sec structures (Extended Data Fig. 4b). Thus, the signal sequence of the substrate may exit through the gap transiently formed between Sec62-TM2 and Sec61α-TM7 during translocation.

Sec62 regulates the gates of Sec61. Three distinct classes of *Sc*Sec (that is, C1, C2 and Sec62−) showed notable conformational differences in the lateral gate (Fig. 2a, and Supplementary Video 1). Although open in all three structures, the extent of the lateral gate opening varies on the ER luminal side, with C1 most open and Sec62− least open. The C2 structure, in which Sec62-TM2 is disengaged, is open to an intermediate degree. The movement is mainly mediated by a rigid body rotation of the TM7, TM8 and the intervening loop (L7/8) of Sec61α (Fig. 2a), which seems to be induced by the interaction between L1/2 of Sec62 and the lateral gate (Fig. 1a–d). Thus, this movement is distinct from the hinge-like motion between the two halves (TM1–5 and TM6–10) of Sec61α which mediates opening of the channel from the fully closed state[6,33–35].

Importantly, the motion of TM7–8 of Sec61α appears to control the position of the plug (Fig. 2b–e). In *Sc*Sec[Sec62−], the plug is clearly visible immediately below the pore constriction ('plug-closed' conformation; Fig. 2b,d and Extended Data Fig. 5). By contrast, in *Sc*Sec[C1], the plug is displaced to a position near the C-terminus of Sec61γ ('plug-open' conformation; Fig. 2c,e), thus opening the pore. The position of the plug in this conformation is consistent with the previous observations that the plug can interact with the TM of the SecE (a prokaryotic equivalent of Sec61γ) subunit[36,37]. In *Sc*Sec[C2], the plug seems disordered,
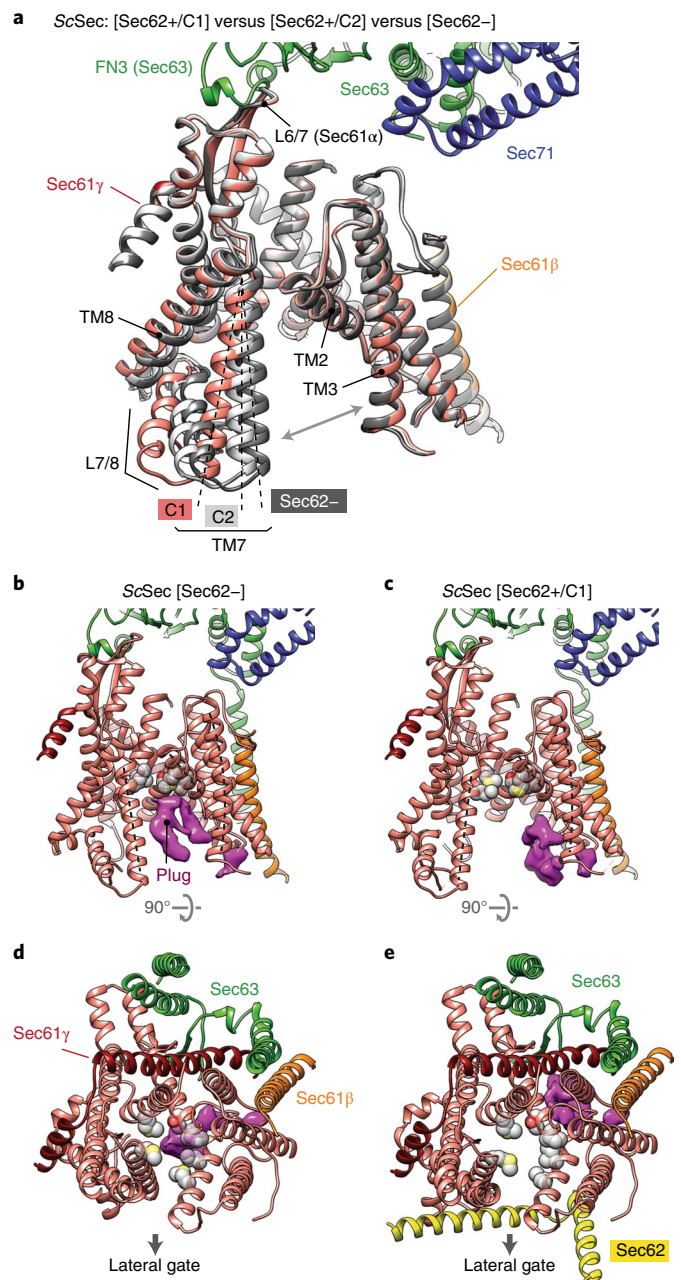

Fig. 2 | Regulation of the lateral and vertical gates by Sec62. a, A comparison of the Sec61 channel conformation between the three *Sc*Sec classes, C1 (in color), C2 (light gray) and Sec62− (dark gray). The dashed lines indicate TM7 of Sec61α and the gray arrows the lateral gate. Sec62 is not shown. **b**–**e**, A comparison of the plug domain (purple density) between Sec62-lacking (left) and -containing *Sc*Sec (right) classes. Gray spheres are the pore ring residues and dashed lines the lateral gate helices (left to right: TM7, TM2 and TM3 of Sec61α). The front views (**b** and **c**) and cytosolic views (**d** and **e**) are shown.

probably because it takes intermediate positions between the two conformations. Similar observations were also made with the *Tl*Sec structures: compared with the Sec62− and ΔSec62 structures, the Sec62+ structure shows a shifted position of Sec61α TM7–8 as in *Sc*Sec[C2] (Extended Data Fig. 6) and concomitant plug mobilization, where 53% and 42% of particles are classified into the plug-closed and -open conformations, respectively (Extended Data Figs. 2 and 6b,c). The plug displacement is
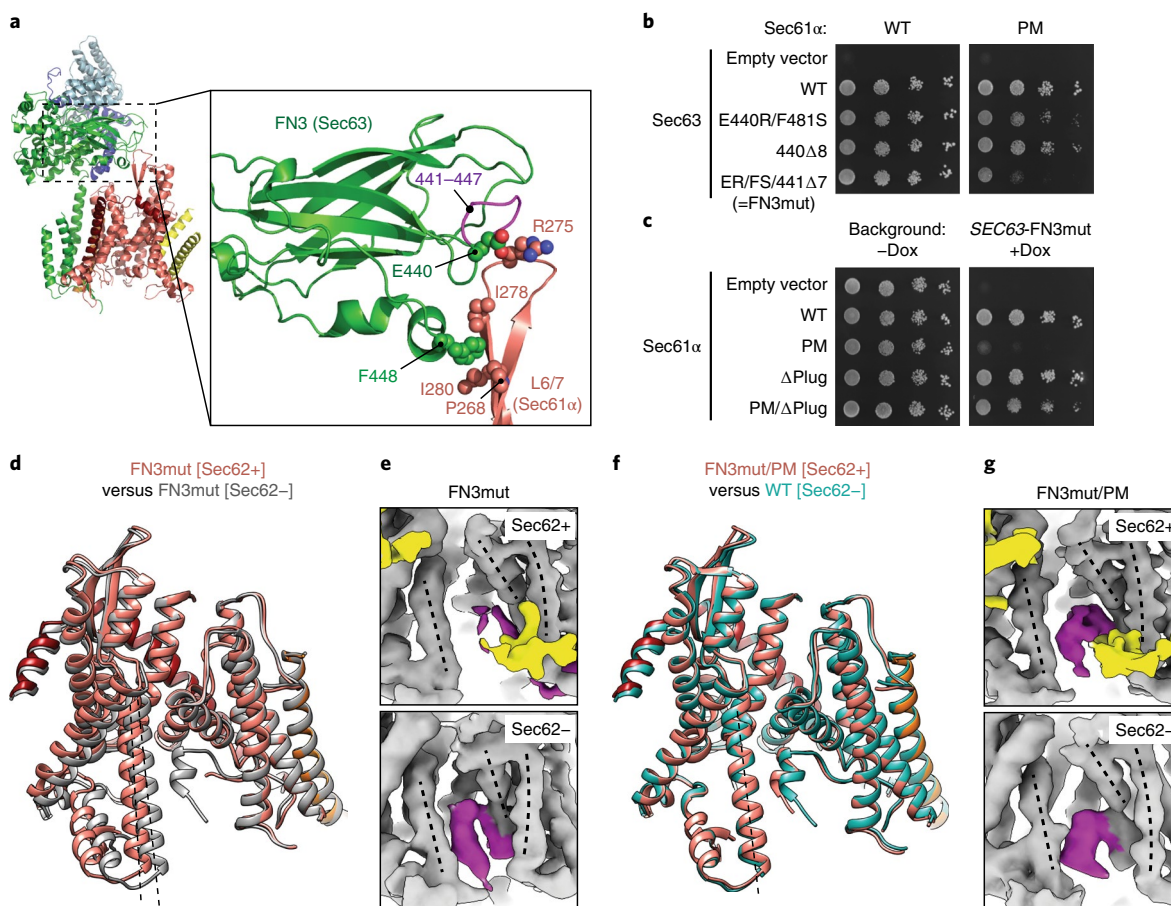
Fig. 3 | Structural and functional analysis of a gating-defective mutant complex. a, The interaction between the FN3 domain of Sec63 and the L6/7 loop of Sec61α (WT ScSec[C1] is shown. Amino acids involved in the interactions are indicated. **b,** Yeast growth complementation experiments (at 30 °C) testing the functionality of indicated FN3 mutants of Sec63 with a background of WT (left) or PM (right) Sec61α. FN3mut refers to a combination of E440R (ER) and F481S (FS) mutations and a deletion of seven amino acids 441–447 (441Δ7). To repress chromosomal WT Sec63 expression (under a tetracycline promoter), doxycycline (Dox) was added. The −Dox control is shown in Extended Data Fig. 7a. **c,** As in **b,** but testing for indicated Sec61α mutants with a background of Sec63-FN3mut as the sole Sec63 copy. The addition of Dox represses chromosomal WT Sec61α expression. **d,** As in Fig. 2a, but with the FN3mut ScSec structures with and without Sec62. **e,** A comparison of the plug domain (purple density) between the FN3mut ScSec structures with and without Sec62 (yellow). Dashed lines are lateral gate helices (left to right: TM7, TM2 and TM3 of Sec61α). **f,** As in **d,** but comparing the Sec62-containing FN3mut/PM structure and the Sec62− class of WT ScSec. **g,** As in **e,** but with the FN3mut/PM ScSec structures. The experiments in **b** and **c** were repeated at least twice with similar results.

probably caused by the Sec62-induced movement of Sec61α-TM7 because the plug interacts with TM7 and L7/8 in the plug-closed conformation[33,38] (Extended Data Fig. 6e).

Partially open Sec61 is inactive. Despite the observed channel gating by Sec62, the physiological importance of this role remained unclear. Without Sec62, the lateral gate can still be opened by Sec63. Even though the pore is blocked by the plug, it has been proposed that insertion of a substrate polypeptide would push the plug away[29]. To investigate the importance of the Sec62-dependent gating, we sought mutations affecting Sec61 gating as ΔSec62 does, but independently of Sec62. If the gating function of Sec62 is essential, such mutations would be expected to compromise cell viability.

We first chose to mutate the fibronectin III (FN3) domain of Sec63, which interacts with the cytosolic loop 6/7 (L6/7) of Sec61α (Fig. 3a). L6/7 also provides a major interaction site for the ribosome in co-translational translocation and the SecA ATPase in bacterial post-translational translocation, and thus has been universally implicated in priming or activating the channel[7,8,21,39,40]. We found that none of the FN3 mutants had a growth defect at 30 °C (Fig. 3b, left panel). Only a mild defect was seen at 37 °C even with the most

severe mutant (FN3mut) (Extended Data Fig. 7b). To understand this unexpectedly weak phenotype, we determined the structure of FN3mut ScSec (Fig. 3d,e, Table 2 and Extended Data Fig. 7c,d). The structure showed that the FN3 domain was indeed disengaged from L6/7 by the mutation, causing ~10° rotation of Sec61 along the membrane normal (Extended Data Fig. 7e,f). Nevertheless, the lateral gate was still open (Fig. 3d). Importantly, the FN3mut complex still exhibited Sec62-induced TM7 movement and plug mobilization (Fig. 3d,e), which may explain the near-WT growth phenotype of the mutant.

Next, we mutated the pore of Sec61α. In closed SecY structures[6–9], the aliphatic amino acids lining the pore constriction (called the pore ring residues) make a hydrophobic interaction with the plug. Compared with other species, the pore ring of ScSec61α appears less hydrophobic[28]. Thus, we reasoned that a mutant with a more hydrophobic pore ring (M90L/T185I/M294I/M450L; collectively denoted pore mutant or PM) might bias the plug toward the closed conformation. In growth complementation assays, the PM itself did not affect cell growth. However, strong synthetic growth impairment was observed when combined with FN3mut (Fig. 3b, right). Importantly, a plug deletion[41] (ΔPlug) could rescue the growth of

Table 2 | Cryo-EM data collection, refinement and validation statistics of mutant *Sc*Sec complexes

	PM *Sc*Sec [Sec62−] (EMD-22778, PDB 7KAO)	PM *Sc*Sec[C1] (EMD-22779, PDB 7KAP)	PM *Sc*Sec [C2] (EMD-22780, PDB 7KAQ)	FN3mut *Sc*Sec[Sec62−] (EMD-22781, PDB 7KAR)	FN3mut *Sc*Sec[Sec62+] (EMD-22782, PDB 7KAS)	PM/FN3mut *Sc*Sec[Sec62−] (EMD-22783, PDB 7KAT)	PM/FN3mut *Sc*Sec[Sec62+] (EMD-22784, PDB 7KAU)	FN3mut/ Δ210−216 *Sc*Sec (EMD-22787, PDB 7KB5)
Data collection and processing								
Magnification	×64,000	×64,000	×64,000	×64,000	×64,000	×64,000	×64,000	×45,000
Voltage (kV)	300	300	300	300	300	300	300	200
Electron exposure (e⁻/Å²)	48.8	48.8	48.8	49.1	49.1	~48–49	~48–49	63
Defocus range (μm)	−1.0 to −2.7	−1.0 to −2.7	−1.0 to −2.7	−0.8 to −2.7	−0.8 to −2.7	−1.1 to −2.2	−1.1 to −2.2	−0.7 to −2.0
Pixel size (Å)	1.15	1.15	1.15	1.19	1.19	1.19	1.19	0.9
Symmetry imposed	C1	C1	C1	C1	C1	C1	C1	C1
Initial particle images (no.)	195,915	195,915	195,915	1,274,219	1,274,219	267,541	267,541	2,270,392
Final particle images (no.)	35,573	17,341	16,679	82,671	119,420	32,704	54,139	257,231
Map resolution (Å)	4.0	4.1	4.0	4.0	3.9	4.4	4.0	3.8
FSC threshold	0.143	0.143	0.143	0.143	0.143	0.143	0.143	0.143
Map resolution range (Å)	3.5–14	3.5–17	3.5–16	3.4–14	3.3–18	3.7–19	3.4–16	3.2–13
Refinement								
Initial model used	PDB 7KAH	PDB 7KAI	PDB 7KAJ	PDB 7KAH	PDB 7KAR	PDB 7KAH	PDB 7KAT	PDB 7KAH
Model resolution (Å)	4.2	4.2	4.2	4.2	4.1	4.5	4.2	4.0
FSC threshold	0.5	0.5	0.5	0.5	0.5	0.5	0.5	0.5
Map sharpening *B* factor (Å²)	50.9	39.3	32.9	74.8	73.8	59.3	58.1	119.3
Model composition								
Nonhydrogen atoms	10,502	10,715	10,753	10,435	10,616	10,431	10,711	9,777
Protein residues	1,349	1,398	1,402	1,341	1,385	1,340	1,396	1,252
B factors (Å²)								
Protein	152	178	187	117	64	255	125	126
R.m.s. deviations								
Bond lengths (Å)	0.003	0.003	0.002	0.003	0.004	0.002	0.003	0.004
Bond angles (°)	0.520	0.519	0.494	0.581	0.596	0.501	0.533	0.626
Validation								
MolProbity score	1.48	1.49	1.46	1.58	1.63	1.37	1.53	1.71
Clashscore	7.65	7.87	7.39	7.84	6.69	6.71	6.26	7.3
Poor rotamers (%)	0	0	0	0	0	0	0	0
Ramachandran plot								
Favored (%)	97.74	97.74	97.75	97.19	96.17	98.10	96.86	95.60
Allowed (%)	2.26	2.26	2.25	2.81	3.83	1.90	3.14	4.40
Disallowed (%)	0	0	0	0	0	0	0	0

the FN3mut/PM, suggesting that the growth inhibition originates from a gating defect (Fig. 3c). Consistent with this idea, the structures of the combined mutant (FN3mut/PM) showed a strong density of the plug in the closed position and no Sec62-dependent movement of lateral gate helices (Fig. 3f,g and Extended Data Fig. 7g). This conformation thereby closely resembles the gating state of *Sc*Sec[Sec62−] despite the presence of Sec62 in front of the lateral gate. On the other hand, the structure of the PM alone still showed Sec62-mediated movements in the lateral gate and plug, similar to the WT (Extended Data Fig. 7h,i). Taken together, these results show that the channel conformation seen in the absence of Sec62 is inactive for post-translational translocation.

Sec62 prevents invasion of lipids into the channel. In addition to the role in channel gating, the ΔSec62 *Tl*Sec structure suggests another function of Sec62− preventing lipids from moving into the

channel. In ΔSec62 *Tl*Sec, strong, well-ordered densities of lipid or detergent tails are visible at the lateral gate (Fig. 4a). The densities are vertically aligned along the hydrophobic groove of the open lateral gate (Fig. 4a and Extended Data Fig. 8a). By contrast, in the Sec62+ structures, only weak fragmented densities were observed (Fig. 4b). In the cytosolic leaflet, a lipid/detergent molecule seems to be accommodated with an outward rotation of the TM2–3 of Sec61α (Extended Data Fig. 8b). Sec62 may inhibit lipids from entering the lateral gate by restricting this movement. In the ER luminal leaflet, the L1/2 of Sec62 seems to sterically block lipids from entering (Fig. 4b). We did not observe a strong lipid/detergent density in the lateral gate of *Sc*Sec[Sec62−], perhaps because of a lower affinity to lipid/detergent. However, one of the previous *Sc*Sec structures[29], the conformation of which resembles the ΔSec62 *Tl*Sec structure, has shown a lipid-like density at the lateral gate and movement of Sec61α TM2–3 similar to ΔSec62 *Tl*Sec (Extended
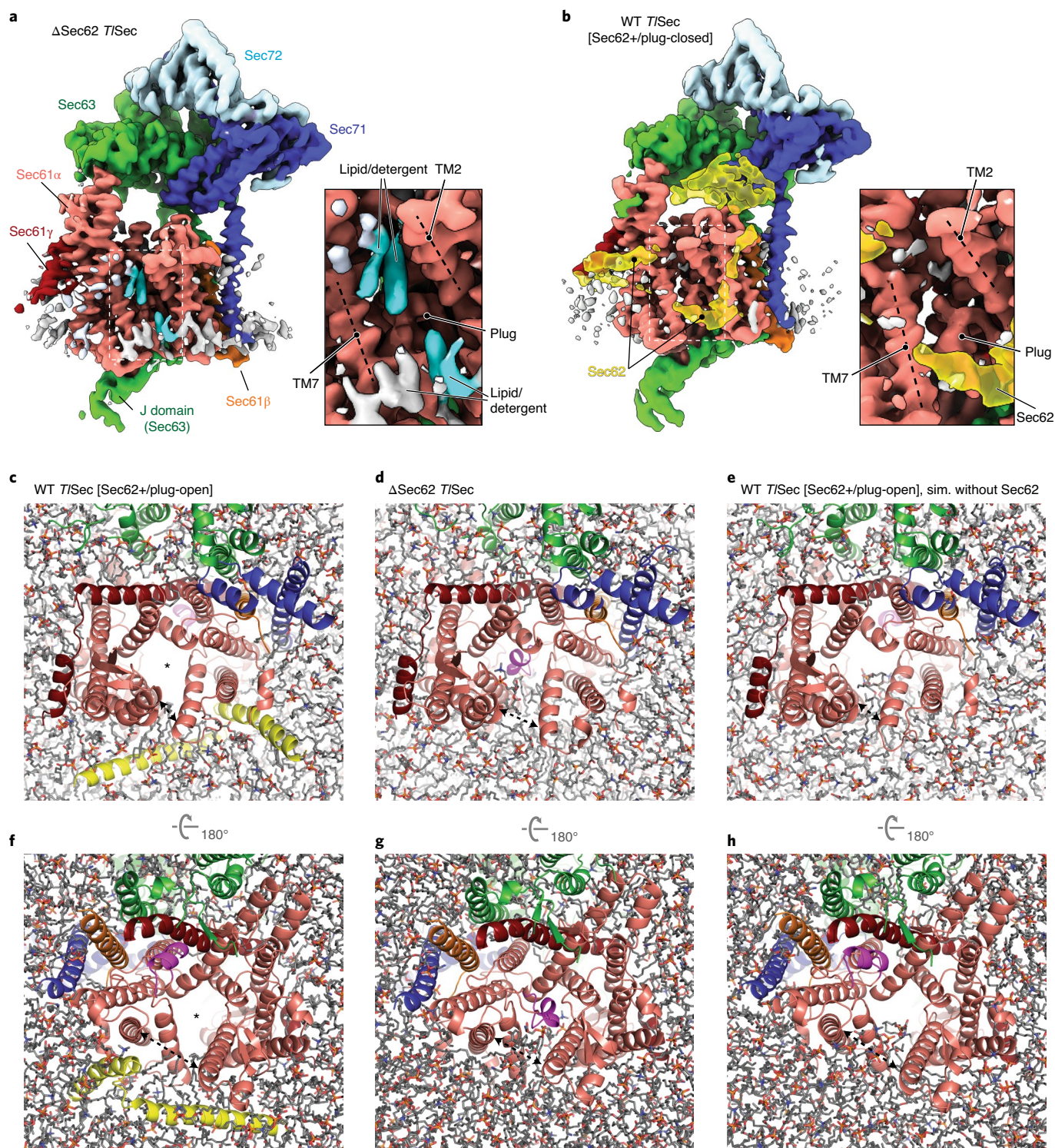
Fig. 4 | Sec62 prevents lipids from invading the Sec61 channel. a, Lipid/detergent molecules at the lateral gate in the *Tl*Sec structure lacking Sec62 (ΔSec62). The left panel is a front view. Non-protein densities are gray. Densities in cyan are lipid/detergent molecules intercalated at the lateral gate. The right panel is an enlarged view of the lateral gate (area indicated by the white dashed box in the left panel). **b**, As in **a**, but with the Sec62+/ plug-closed class of WT *Tl*Sec. We note that, similarly, the Sec62+/plug-open class does not show lipid/detergent densities at the lateral gate. **c–h**, All-atom MD simulations with indicated *Tl*Sec structures in a model membrane (**c** and **f**, WT *Tl*Sec[Sec62+/plug-open]; **d** and **g**, ΔSec62 *Tl*Sec; **e** and **h**, WT *Tl*Sec[Sec62+/plug-open] but without Sec62). The Sec complex is shown in ribbon representation in the same colors as in **a** and **b**. Lipids are shown in stick representation; **c–e** are views from the cytosol and **f–h** are views from the ER lumen. In **c** and **f**, the translocation pore is marked by an asterisk. The lateral gate openings are indicated by a dashed arrow. The frames are from 200 ns after the initiation of simulations.

Data Fig. 8c,d). Collectively, these observations suggest that, in the absence of Sec62, lipid molecules may penetrate the lateral gate that is opened by Sec63.

To further investigate a role of Sec62 in blocking lipid penetration, we performed 200-ns all-atom MD simulations (Fig. 4c–h and Extended Data Fig. 9). In simulations of the Sec62-containing
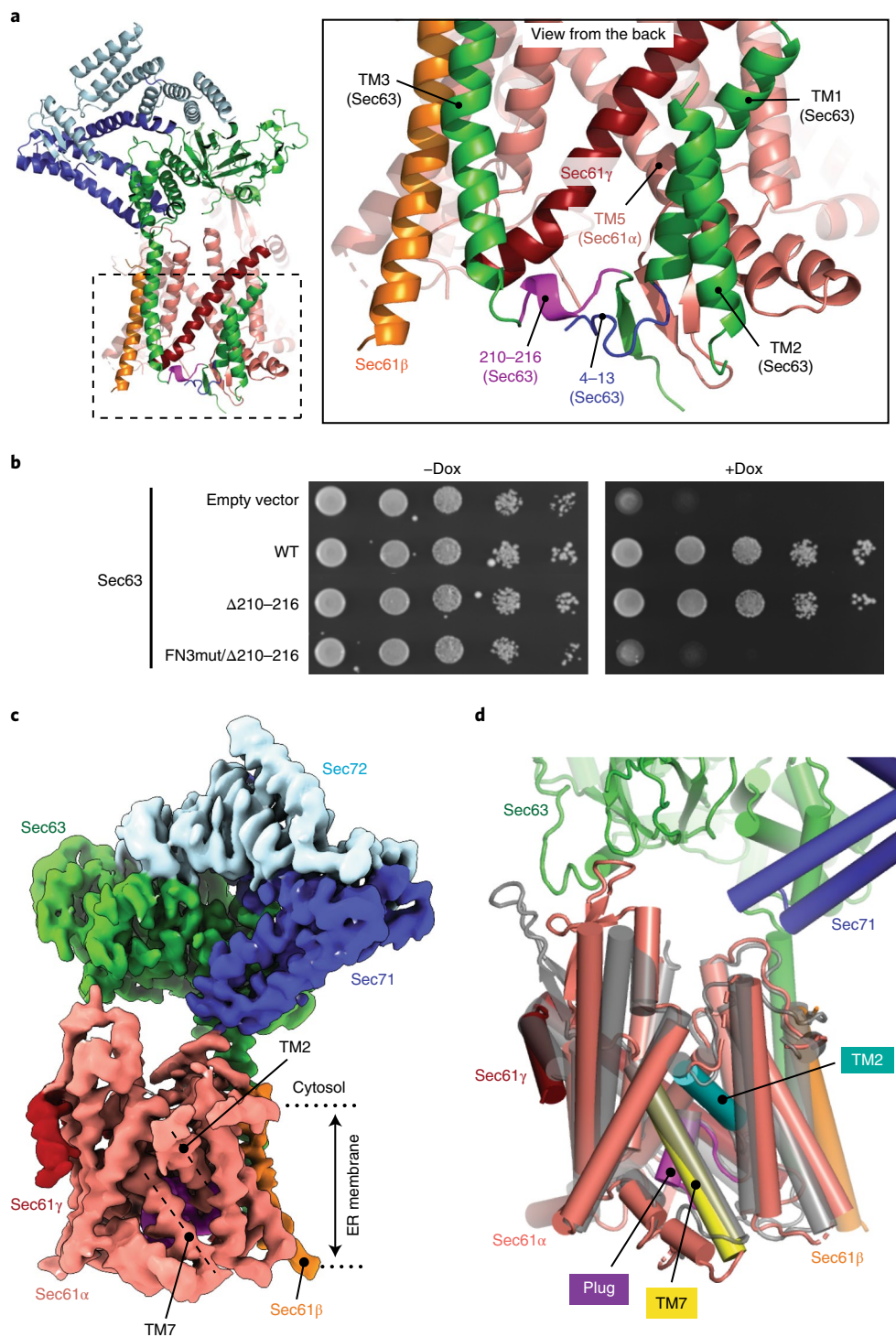
Fig. 5 | The structure of a fully closed Sec complex. a, The interaction between Sec61 and Sec63 in the ER lumen (view from the back). The N-terminal segment (positions 4–13) and the segment preceding TM3 (positions 210–216) of Sec63 are in blue and purple, respectively. The ScSec[C1] structure is shown. **b**, Yeast growth complementation (at 30 °C) testing the functionality of the indicated Sec63 mutants. The addition of Dox represses chromosomal WT Sec63 expression. The experiments were repeated twice with similar results. **c**, The 3.8-Å-resolution cryo-EM structure of the ScSec complex containing FN3mut/Δ210–216 double-mutant Sec63. The lateral gate helices TM2 and TM7 are indicated. **d**, As in **c**, but showing the atomic model of the Sec61 complex. For comparison, the closed *Methanocaldococcus jannaschii* SecY structure (PDB 1RH5; semitransparent gray) is superimposed.

structures (that is, WT *Tl*Sec[Sec62+/plug-open] and WT *Sc*Sec[C1] and [C2]), the translocation pore largely remained unobstructed and devoid of lipids (Fig. 4c,f, Extended Data Fig. 9a–d and Supplementary Videos 2–4). Only one phospholipid molecule partially penetrated the lateral gate of *Sc*Sec in the cytosolic leaflet of

the membrane, with its aliphatic tails remaining outside (Extended Data Fig. 9a–d); further incursion is unlikely because the interior of the cytosolic half of the channel is highly polar[42]. Notably, no lipids penetrated the channel in the luminal leaflet during the entire duration of the simulations, despite a larger opening (~20 Å in *Tl*Sec
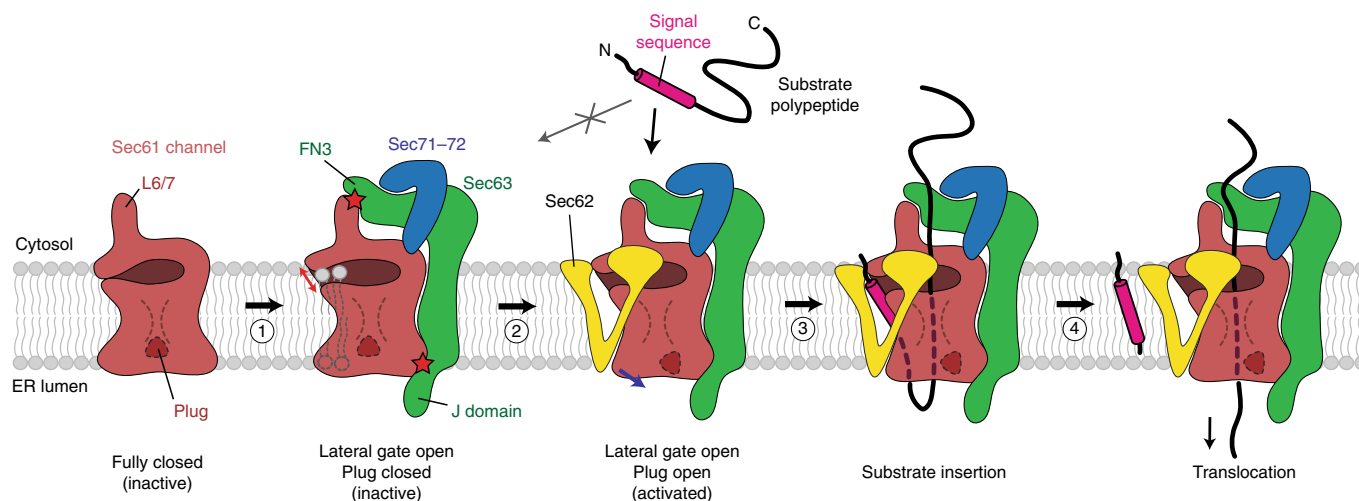
Fig. 6 | A model for the activation of the Sec61 channel by Sec62 and Sec63. The Sec61 channel alone assumes a fully closed conformation (the leftmost cartoon). Step 1: association of Sec63 opens the lateral gate (indicated by a red arrow) through interactions with Sec61 in both the cytosol and the ER lumen (indicated by red stars). The channel in this conformation is inactive due to the closed state of the plug domain. In addition, without Sec62, lipids may enter the open lateral gate. Step 2: Sec62 interacts with the lateral gate of Sec61 and further opens the lateral gate (blue arrow), which results in opening of the plug. The V-shaped transmembrane domain of Sec62 excludes lipids from the channel. Step 3: a substrate polypeptide inserts into the open pore of the channel as a loop with the signal sequence sitting at the lateral gate. Step 4: the signal sequence is cleaved by the signal peptidase (not shown), and the polypeptide is translocated into the ER lumen. For simplicity, the BiP ATPase, which drives translocation by interactions with the polypeptide and J domain, is not shown.

and ~30 Å in *Sc*Sec) between TM3 and TM7 of Sec61α (Fig. 4f and Extended Data Fig. 9b,d). As the plug is displaced in these structures, the luminal funnel of Sec61α remained completely unoccupied. By contrast, simulations of the Sec62-lacking structures (ΔSec62 *Tl*Sec and *Sc*Sec[Sec62−]) showed substantially deeper penetration of lipid molecules into the lateral gate (Fig. 4d,g, Extended Data Fig. 9e,f and Supplementary Videos 5 and 6). In both the cytosolic and luminal leaflets of the membrane, the lateral gate became occupied with lipids within ~80 ns. These results are consistent with the lipid/detergent densities seen in the cryo-EM structure of ΔSec62 *Tl*Sec.

Our cryo-EM structures and MD simulations suggested that the V-shaped transmembrane domain of Sec62 effectively blocks lipids from entering the open lateral gate, particularly on the ER luminal leaflet. We thus hypothesized that, without Sec62, the pore may be invaded by lipids if both the lateral gate and the plug remain open. We tested this idea by running another set of MD simulations on *Tl*Sec[Sec62+] and *Sc*Sec[C1] but excluding the Sec62 subunit (Fig. 4e,h, Extended Data Fig. 9g,h and Supplementary Videos 7 and 8). The results indeed show that, in both *Tl*Sec and *Sc*Sec, lipids invaded the pore mainly from the luminal leaflet, substantially obstructing the translocation pathway. It is probable that lipid molecules occupying the pore would inhibit insertion of substrate polypeptides. Thus, Sec62 seems to play an important role in maintaining the functionality of Sec61 by keeping lipids away from the open channel.

Mechanism of Sec61 gating by Sec63. One unexpected finding was that the FN3-L6/7 interaction was dispensable for the protein translocation function of the Sec complex. This indicates that there must be another mechanism for Sec63 to open the lateral gate. Besides the FN3 domain, Sec63 forms major contacts with Sec61 through two other parts: TM3, which anchors Sec63 to the Sec61 complex, and a short ER luminal segment (residues 210–216) preceding TM3, which, together with the N-terminal segment of Sec63, interacts with a crevice on the back of the channel (opposite the lateral gate; Fig. 5a). We reasoned that the latter interaction might control lateral gating through a lever-like mechanism. In the WT background, replacement of this segment with a glycine/serine linker (Δ210–216)

alone did not cause growth inhibition (Fig. 5b). However, when combined with FN3mut, cells did not grow (Fig. 5b).

To understand the structural basis of this synthetic defect, we determined the structure of the FN3mut/Δ210–216 *Sc*Sec complex (Fig. 5c and Extended Data Fig. 10) The structure showed that, indeed, both the lateral and the vertical gates of the Sec61 channel are completely closed, resembling the idle archaeal SecY channel structure[6] (Fig. 5c and Extended Data Fig. 10). This demonstrates that Sec63 uses both its cytosolic and luminal domains to open the lateral gate in a two-pronged mechanism. The C-terminal cytosolic domain of Sec63 (following TM3) and Sec71–Sec72 are still attached to Sec61 through TM3. However, most of the parts preceding TM3 were invisible due to increased flexibility. Importantly, Sec62 was no longer visible either, despite copurification with the complex (Fig. 5c and Extended Data Fig. 10a). Sec62 is probably associated with Sec63 through an electrostatic interaction with the C-terminal tail of Sec63 (refs. [30,43]) (Fig. 1d), but it seems to no longer bind to the lateral gate due to structural incompatibility with the closed gate. Therefore, the lateral gate must be first opened by Sec63 before Sec62 can activate the channel for protein translocation.

Discussion

In summary, our study defines the functions of Sec62 and reveals the mechanism by which Sec63 and Sec62 regulate the gates of the Sec61 channel. The function of Sec62 had been elusive for three decades since its discovery as an essential component in eukaryotic post-translational translocation[22,23,44]. Our study shows that, once the lateral gate of the Sec61 channel is opened by Sec63, Sec62 fully activates the channel by further mobilizing the plug domain (Fig. 6). At the same time, Sec62 seems to prevent lipids from penetrating the channel interior through the open lateral gate by forming a barrier in front of the lateral gate. Such lipid penetration into the lateral gate and translocation pore would probably impair the protein translocation activity by competitively inhibiting insertion of polypeptide substrates into the channel. The lipids may also affect movements of polypeptides in later stages of protein translocation. The V-shaped structure formed by the transmembrane domain of Sec62 is rather dynamic with respect to the rest of the complex and

loosely associated with the lateral gate, as suggested by its relatively low-resolution densities in our cryo-EM maps. This flexibility may be important for insertion of signal sequences into and its egress from the lateral gate. It is also possible that the movement of Sec62 is modulated by binding of signal sequences and other protein translocation factors (for example, BiP) to the Sec61 channel.

The fully open conformation of the WT Sec complexes observed in our cryo-EM structures probably represents a resting state before substrate engagement. Although the channel's conformation and its dynamics in the native membrane environment remain to be determined, we speculate that this open state is probably a predominant form in the native ER membrane, based on the stable association of Sec61, Sec62 and Sec63. A pre-opened Sec61 channel in the post-translational complex contrasts with a relatively closed Sec61 channel seen with resting co-translational complexes, where the lateral gate is only marginally open, and the plug domain remains in the closed position[8]. It has been generally thought that, during initial substrate engagement, the Sec61 channel would be opened by a hydrophobic interaction between the signal sequence (or TM helix) and the lateral gate[2,8,11,14,45]. Our mutagenesis analysis, however, indicates that such a partially open state, similar to the one induced by Sec63 alone, is insufficient for post-translational protein translocation. This is probably because the plug domain in the closed position would impose too high an energy barrier for post-translational polypeptide substrates to insert into the pore.

Many post-translational substrates are known to contain a signal sequence with relatively lower hydrophobicity[15]. Eukaryotic post-translational substrates are also expected to interact more transiently with Sec61 during initial insertion, because they are not tethered to the ribosome as in the co-translational mode or to the SecA ATPase as in the bacterial post-translational mode. These features of substrates for the Sec complex may require both the lateral and the vertical gates of the channel to be pre-opened for efficient insertion. A reduced energy barrier for substrate insertion by pre-opening the gates would allow polypeptides to promptly engage with the Sec61 complex, without which polypeptides may lose translocation competency because of premature folding or aggregation. Maintaining a stably open conformation by Sec63 and Sec62 may also be important for subsequent translocation steps because it may reduce friction in polypeptide movements. Our structural analysis shows that Sec63 and Sec62 open the gates of the Sec61 channel in a stepwise fashion to activate the channel, explaining their essentiality in cell viability. Given the high degree of sequence conservation of these components, the gating mechanism we discovered on the present study is probably conserved across all eukaryotic species.

Online content

Any methods, additional references, Nature Research reporting summaries, source data, extended data, supplementary information, acknowledgements, peer review information; details of author contributions and competing interests; and statements of data and code availability are available at https://doi.org/10.1038/s41594-020-00541-x.

References

1. Rapoport, T. A., Li, L. & Park, E. Structural and mechanistic insights into protein translocation. *Annu. Rev. Cell Dev. Biol.* **33**, 369–390 (2017).
2. Voorhees, R. M. & Hegde, R. S. Toward a structural understanding of co-translational protein translocation. *Curr. Opin. Cell Biol.* **41**, 91–99 (2016).
3. Collinson, I., Corey, R. A. & Allen, W. J. Channel crossing: how are proteins shipped across the bacterial plasma membrane? *Phil. Trans. R. Soc. Lond. B Biol. Sci.* **370**, 20150025 (2015).
4. Tsirigotaki, A., De Geyter, J., Sostaric, N., Economou, A. & Karamanou, S. Protein export through the bacterial Sec pathway. *Nat. Rev. Microbiol.* **15**, 21–36 (2017).
5. Seinen, A. B. & Driessen, A. J. M. Single-molecule studies on the protein translocon. *Annu. Rev. Biophys.* **48**, 185–207 (2019).
6. Van den Berg, B. et al. X-ray structure of a protein-conducting channel. *Nature* **427**, 36–44 (2004).
7. Tsukazaki, T. et al. Conformational transition of sec machinery inferred from bacterial SecYE structures. *Nature* **455**, 988–991 (2008).
8. Voorhees, R. M., Fernandez, I. S., Scheres, S. H. & Hegde, R. S. Structure of the mammalian ribosome–Sec61 complex to 3.4 Å resolution. *Cell* **157**, 1632–1643 (2014).
9. Tanaka, Y. et al. Crystal structures of SecYEG in lipidic cubic phase elucidate a precise resting and a peptide-bound state. *Cell Rep.* **13**, 1561–1568 (2015).
10. Li, L. et al. Crystal structure of a substrate-engaged SecY protein-translocation channel. *Nature* **531**, 395–399 (2016).
11. Voorhees, R. M. & Hegde, R. S. Structure of the Sec61 channel opened by a signal sequence. *Science* **351**, 88–91 (2016).
12. Ma, C. et al. Structure of the substrate-engaged SecA–SecY protein translocation machine. *Nat. Commun.* **10**, 2872 (2019).
13. Braunger, K. et al. Structural basis for coupling protein transport and N-glycosylation at the mammalian endoplasmic reticulum. *Science* **360**, 215–219 (2018).
14. Gogala, M. et al. Structures of the Sec61 complex engaged in nascent peptide translocation or membrane insertion. *Nature* **506**, 107–110 (2014).
15. Ng, D. T., Brown, J. D. & Walter, P. Signal sequences specify the targeting route to the endoplasmic reticulum membrane. *J. Cell Biol.* **134**, 269–278 (1996).
16. Muller, G. & Zimmermann, R. Import of honeybee prepromelittin into the endoplasmic reticulum: structural basis for independence of SRP and docking protein. *EMBO J.* **6**, 2099–2107 (1987).
17. Lakkaraju, A. K. et al. Efficient secretion of small proteins in mammalian cells relies on Sec62-dependent posttranslational translocation. *Mol. Biol. Cell* **23**, 2712–2722 (2012).
18. Chen, L., Rhoads, D. & Tai, P. C. Alkaline phosphatase and OmpA protein can be translocated posttranslationally into membrane vesicles of *Escherichia coli*. *J. Bacteriol.* **161**, 973–980 (1985).
19. Cabelli, R. J., Chen, L., Tai, P. C. & Oliver, D. B. SecA protein is required for secretory protein translocation into *E. coli* membrane vesicles. *Cell* **55**, 683–692 (1988).
20. Brundage, L., Hendrick, J. P., Schiebel, E., Driessen, A. J. & Wickner, W. The purified *E. coli* integral membrane protein SecY/E is sufficient for reconstitution of SecA-dependent precursor protein translocation. *Cell* **62**, 649–657 (1990).
21. Zimmer, J., Nam, Y. & Rapoport, T. A. Structure of a complex of the ATPase SecA and the protein-translocation channel. *Nature* **455**, 936–943 (2008).
22. Rothblatt, J. A., Deshaies, R. J., Sanders, S. L., Daum, G. & Schekman, R. Multiple genes are required for proper insertion of secretory proteins into the endoplasmic reticulum in yeast. *J. Cell Biol.* **109**, 2641–2652 (1989).
23. Deshaies, R. J., Sanders, S. L., Feldheim, D. A. & Schekman, R. Assembly of yeast Sec proteins involved in translocation into the endoplasmic reticulum into a membrane-bound multisubunit complex. *Nature* **349**, 806–808 (1991).
24. Meyer, H. A. et al. Mammalian Sec61 is associated with Sec62 and Sec63. *J. Biol. Chem.* **275**, 14550–14557 (2000).
25. Tyedmers, J. et al. Homologs of the yeast Sec complex subunits Sec62p and Sec63p are abundant proteins in dog pancreas microsomes. *Proc. Natl Acad. Sci. USA* **97**, 7214–7219 (2000).
26. Feldheim, D., Rothblatt, J. & Schekman, R. Topology and functional domains of Sec63p, an endoplasmic reticulum membrane protein required for secretory protein translocation. *Mol. Cell Biol.* **12**, 3288–3296 (1992).
27. Matlack, K. E., Misselwitz, B., Plath, K. & Rapoport, T. A. BiP acts as a molecular ratchet during posttranslational transport of prepro-α factor across the ER membrane. *Cell* **97**, 553–564 (1999).
28. Itskanov, S. & Park, E. Structure of the posttranslational Sec protein-translocation channel complex from yeast. *Science* **363**, 84–87 (2019).
29. Wu, X., Cabanos, C. & Rapoport, T. A. Structure of the post-translational protein translocation machinery of the ER membrane. *Nature* **566**, 136–139 (2019).
30. Wittke, S., Dunnwald, M. & Johnsson, N. Sec62p, a component of the endoplasmic reticulum protein translocation machinery, contains multiple binding sites for the Sec-complex. *Mol. Biol. Cell* **11**, 3859–3871 (2000).
31. Shaw, A. S., Rottier, P. J. & Rose, J. K. Evidence for the loop model of signal-sequence insertion into the endoplasmic reticulum. *Proc. Natl Acad. Sci. USA* **85**, 7592–7596 (1988).
32. Paetzel, M., Karla, A., Strynadka, N. C. & Dalbey, R. E. Signal peptidases. *Chem. Rev.* **102**, 4549–4580 (2002).
33. Egea, P. F. & Stroud, R. M. Lateral opening of a translocon upon entry of protein suggests the mechanism of insertion into membranes. *Proc. Natl Acad. Sci. USA* **107**, 17182–17187 (2010).

34. Park, E. et al. Structure of the SecY channel during initiation of protein translocation. *Nature* **506**, 102–106 (2014).
35. Pfeffer, S. et al. Structure of the native Sec61 protein-conducting channel. *Nat. Commun.* **6**, 8403 (2015).
36. Flower, A. M., Osborne, R. S. & Silhavy, T. J. The allele-specific synthetic lethality of prlA-prlG double mutants predicts interactive domains of SecY and SecE. *EMBO J.* **14**, 884–893 (1995).
37. Harris, C. R. & Silhavy, T. J. Mapping an interface of SecY (PrlA) and SecE (PrlG) by using synthetic phenotypes and in vivo cross-linking. *J. Bacteriol.* **181**, 3438–3444 (1999).
38. Hizlan, D. et al. Structure of the SecY complex unlocked by a preprotein mimic. *Cell Rep.* **1**, 21–28 (2012).
39. Cheng, Z., Jiang, Y., Mandon, E. C. & Gilmore, R. Identification of cytoplasmic residues of Sec61p involved in ribosome binding and cotranslational translocation. *J. Cell Biol.* **168**, 67–77 (2005).
40. Becker, T. et al. Structure of monomeric yeast and mammalian Sec61 complexes interacting with the translating ribosome. *Science* **326**, 1369–1373 (2009).
41. Junne, T., Schwede, T., Goder, V. & Spiess, M. The plug domain of yeast Sec61p is important for efficient protein translocation, but is not essential for cell viability. *Mol. Biol. Cell* **17**, 4063–4068 (2006).
42. Gumbart, J., Chipot, C. & Schulten, K. Free energy of nascent-chain folding in the translocon. *J. Am. Chem. Soc.* **133**, 7602–7607 (2011).
43. Willer, M., Jermy, A. J., Young, B. P. & Stirling, C. J. Identification of novel protein–protein interactions at the cytosolic surface of the Sec63 complex in the yeast ER membrane. *Yeast* **20**, 133–148 (2003).
44. Deshaies, R. J. & Schekman, R. SEC62 encodes a putative membrane protein required for protein translocation into the yeast endoplasmic reticulum. *J. Cell Biol.* **109**, 2653–2664 (1989).
45. Kater, L. et al. Partially inserted nascent chain unzips the lateral gate of the Sec translocon. *EMBO Rep.* **20**, e48191 (2019).

Methods

Yeast strains. A list of yeast strains used in this study is given in Supplementary Table 1.

The yeast strain (ySI7) used for purification of the WT *Sc*Sec complex has been described previously[28]. Briefly, this strain expresses a fusion protein of Sec61β (Sbh1), Sec63 and a green fluorescent protein (GFP) from the genomic *SEC63* locus under the endogenous promoter of *SEC63* (the endogenous *SBH1* copy is deleted). The C-terminus of Sbh1p and the N-terminus of Sec63 are separated by a glycine–serine linker that is 15 amino acids long. There is a flexible linker containing a tobacco etch virus (TEV) cleavage sequence between the C-terminus of Sec63 and GFP.

To enable purification of the PM *Sc*Sec complex, we generated strain ySI8 by modifying ySI7. We first clone the *SEC61* gene (from 1,965 bp upstream to 668 bp downstream of the Sec61-coding sequence (CDS) of BY4741) into a pBlueScript-derived cloning vector (comprising a pUC origin and an ampicillin resistance gene). We then inserted a *LEU2* selection marker cassette (amplified by PCR using pYTK075 as a template, a forward primer: 5′-agctaaataagatctTCGAGGAGAACTTCTAGTATATCTACATAC-3′, and a reverse primer: 5′- tatatataggagctcCTGCCTATTTAACGCCAAC-3′, upper case for *LEU2*-specific sequences and lower case for *SEC61*-specific sequences) was inserted between 125 bp and 126 bp downstream of the Sec61 stop codon by In-Fusion cloning (Takara Bio). Pore mutations (M90L/T185I/M294I/M450L) were introduced to Sec61 by site-specific mutagenesis. The resulting plasmid was then linearized by cutting the plasmid backbone with *Not*I. The DNA fragment was introduced into ySI7 by a standard lithium acetate/poly(ethylene glycol) transformation protocol. Recombinants were selected on a leucine drop-out synthetic complete (SC(−Leu)) agar medium. Incorporation of the mutations was verified by PCR and Sanger sequencing of single colonies.

To purify the FN3mut *Sc*Sec complex, we generated strain ySI73 by modifying strain TH_5187 (Horizon Discovery) from the Hughes' collection[46], where the expression of chromosomal Sec63 is under the control of a tetracycline-repressible promoter. First, the endogenous copy of *SBH1* of TH_5187 was replaced with a hygromycin resistance marker (hphMX) cassette. An hphMX cassette fragment was amplified by PCR using pFA6a-hphMX6 (ref. [47]) as a template (forward primer: 5′-gggaaaagatttcaaccaccacttcaaaacaccacactctacctcctaccatactccataAGCTTGCCT CGTCCCC-3′; reverse primer: 5′-tagtcttgttttgtcaaataggtggatgaaaagctgaatcattactg aagaaaattcttaCAGTATAGCGACCAGCATTCAC-3′; upper case for vector specific sequences and lower case for sequences homologous to yeast chromosomal sequences). The DNA fragment was transformed into TH_5187. Single colonies were isolated from YPD (1% yeast extract, 2% peptone, 2% glucose) agar plates containing 400 μg ml⁻¹ of hygromycin (Gold Biotechnology) and integration was verified by PCR. The resulting strain (ySI48) was then further modified by integration of the FN3mut Sec63 construct into the *HO* locus using the transforming plasmid pSI74 (see below) linearized at *Hind*III, which cuts at the *Escherichia coli* kanamycin resistance marker (KanMX). Transformed cells were selected on SC(−Leu) agar medium and integration was verified by PCR.

For purification of the FN3mut/PM *Sc*Sec complex, we used strain ySI74. To generate ySI74, we first modified TH_5187 to contain the pore mutations in the *SEC61* gene, similarly as described above for ySI8, but using a nourseothricin resistance cassette (natMX6) instead of the *LEU2* marker. The natMX6 cassette was amplified from pFA6a-natMX6 (ref. [47]) and inserted into the pBlueScript-Sec61 plasmid at 125 bp downstream of the Sec61 stop codon. After transformation of the linearized plasmid, recombinants were selected on YPD agar plates containing 100 μg ml⁻¹ of nourseothricin (Gold Biotechnology), resulting in ySI42. Subsequently, *SBH1* deletion and Sec63-FN3mut mutation were introduced to the strain as described for ySI73.

For purification of the FN3mut/Δ210–216 *Sc*Sec complex, we used strain ySI112. To generate ySI112 we modified strain ySI48 (TH_5187 *sbh1Δ::hphMX6*) by integration of the FM3mut/Δ210–216 Sec63 construct into the *HO* locus using the transforming plasmid pSI120 (see below) linearized with *Hind*III.

The WT and mutant *Tl*Sec complexes were expressed using the yeast strains ySI67 (for WT), ySI77 (for ΔSec62) and ySI113 (for Δanchor). These strains were generated from the parental strain yMLT62 (a gift from J. Thorner[48]), which expresses the β-estradiol-responsive chimeric transcription activator Gal4dbd.ER.VP16. All *Tl*Sec subunits were co-expressed with an integration vector (pYTK-e101) generated using MoClo Yeast ToolKit (YTK)[49] (see below). Expression of each gene is driven by a GAL1 promoter. The vector pYTK-e101 contains a natMX6 marker and *URA3* homology sequences for chromosomal integration; pYTK-e101 encoding WT (pSI65) or mutant *Tl*Sec (pSI87 for ΔSec62 and pSI94 for Δanchor) was linearized with *Not*I and transformed into yMLT62. Recombinants were selected by growth on YPD agar plates containing 100 μg ml⁻¹ of nourseothricin. Integration was verified by PCR as described[49].

For yeast growth complementation assays for Sec62, we generated ySI62, the chromosomal Sec62 expression of which can be repressed in the presence of doxycycline. The tetracycline response element (TRE), as well as the upstream kanMX cassette, were PCR amplified from genomic DNA of TH_5187 with primers containing 60-bp overhangs homologous to the N-terminus of Sec62 (forward primer: 5′- gacggaatagacgtgtcgttttcccaatactggcatacaaatcaagagggagaagagt ggGGCGTTAGTATCGAATCG-3′; reverse primer: 5′- tgtagcagatccgccattga

cactagcacctgcattgctacctggacctacggctgacatGGATCCCCCGAATTG-3′; upper case for sequence specific to TRE-kanMX and lower case for sequences homologous to yeast chromosomal sequences). The amplicon was then transformed into the strain R1158 (the parental strain for TH_5187) which contains the 'tet activator'. Transformed cells were selected on 300 μg ml⁻¹ of G418 (Fisher Chemical) containing YPD agar plates, and integration was verified by PCR.

Strain ySI89 was used for complementation assays testing synthetic growth defects of FN3mut Sec63 and Sec61 mutants (Fig. 3c). To generate this strain, TH_4087 (Hughes' strain with the chromosomal *SEC61* expressing under a tetracycline-repressible promoter) was modified such that its endogenous Sec63 was mutated to FN3mut. A DNA segment encoding part of the FN3mut Sec63 was amplified by PCR from plasmid pSI16 (from amino acid 164 to the stop codon) and inserted into pFA6a-natMX6 immediately before an ADH1 terminator, which precedes the natMX6 cassette. The resulting construct was amplified by PCR to include 773 bp upstream of the first mutated amino acid (E440R) and 50 bp of the 3′-untranslated region of the *SEC63* locus (forward primer: 5′-CCCTTACTGACGAATTGGTTAGGC-3′; reverse primer: 5′-atgtatctattttttataaagatgaaatatatacgtctaagagctaaaatgGGCCGCATAGGCCACTAG -3′; upper case for sequence specific to the plasmid and lower case for sequences homologous to yeast chromosomal sequence). The amplicon was transformed into TH_4087 and selected on 100 μg ml⁻¹ of nourseothricin containing YPD agar plates. Incorporation of the mutation was verified using Sanger sequencing.

Plasmids. A list of plasmids used in this study is given in Supplementary Table 1.

The integration vectors pYTK-e101 and pYTK-e106, and CEN/ARS plasmid pYTK-e112, were generated using Golden Gate *Bsa*I assembly of parts from MoClo YTK[49] (for pYTK-e101, part nos. were 8, 47, 73, 78, 86, 90 and 92; for pYTK-e106, part nos. were 8, 47, 73, 75, 88, 90 and 94; for pYTK-e112, part nos. were 8, 47, 73, 75, 81 and 84). The vector pYTK-e101 contains a natMX6 marker and integrates into the *URA3* locus. The vector pYTK-e106 contains a *LEU2* auxotroph marker and integrates into the *HO* locus.

The *Tl*Sec-expressing pYTK-e101 plasmids were generated using MoClo YTK as follows: first, gene fragments encoding *Tl*Sec subunits were chemically synthesized based on protein sequences of *T. lanuginosus* American Type Culture Collection 2000065 (https://gb.fungalgenomics.ca) and cloned into the YTK entry vector pYTK001 (ref. [49]). Codons were optimized for yeast. In the case of the Sec63 and Sec61β subunits, a fusion construct (*Tl*Sec61β–GGSGGSGGSGGSGGS–TEV–GFP) was synthesized similarly to the expression of the *Sc*Sec complex. Each synthesized CDS was then cloned into the pYTK095 vector[49] as an expression cassette, together with a *GAL1* inducible promoter, an *ENO1* terminator and connector parts by Golden Gate *Bsa*I assembly. Subsequently, the multigene expression construct was generated by Golden Gate *Bsm*BI assembly of the pYTK095 plasmids and pYTK-e101, resulting in pSI65 (the *Sec* gene placed in tandem in the following order: *Tl*Sec61α, *Tl*Sec61γ, *Tl*Sec62, *Tl*Sec61β-*Tl*Sec63-GFP, *Tl*Sec71 and *Tl*Sec72). For ΔSec62 *Tl*Sec (plasmid pSI87), pYTK095-*Tl*Sec62 was replaced by a nonexpressing spacer cassette in the *Bsm*BI assembly. For Δanchor *Tl*Sec (plasmid pSI94), amino acid residues N³¹⁹LF… WNE³³⁸ of *Tl*Sec62 were replaced with a Gly/Ser linker (GGSGGSGGS) before the multigene *Bsm*BI assembly.

For expression of Sec63-mutant *Sc*Sec complexes (FN3mut and FN3mut/ Δ210–216), WT *Sc*Sec63 was first amplified from genomic DNA of BY4741 by PCR to include the endogenous promoter and terminator (187 bp upstream and 97 bp downstream of the CDS) and cloned into pYTK-e112 between the two *Bsa*I sites (pSI5). This plasmid was then further modified to have Sbh1 and GFP flanking Sec63 as in other Sbh1–Sec63 fusion constructs (that is, Sbh1– GGSGGSGGSGGSGGS–Sec63–TEV–GFP). Then FN3mut (E440R/F481S/Δ441– 447) or FN3mut/Δ210–216 (FN3mut and residues L²¹⁰PRFLVD²¹⁶, replaced with SGSGGGSG) mutations were introduced by site-specific mutagenesis. For generation of strains ySI74 and ySI112 (chromosomal integration of mutant Sec63 to the *HO* locus), the expression cassette for Sbh1–Sec63–GFP was transferred to pYTK-e106 by restriction digestion and ligation.

For growth complementation assays, *SEC61* (710 bp upstream to 264 bp downstream of CDS) and *SEC62* (251 bp upstream to 123 bp downstream of CDS) were amplified by PCR using genomic DNA of BY4741 and cloned into pYTK-e112, resulting in pSI123 and pSI39, respectively. Plasmids used for growth complementation assays of Sec63 mutants were derived from pSI5 (see above) by adding a TEV–GFP tag at the C-terminus of Sec63 (the Sbh1 fusion was not introduced, and thus the constructs have the native N-terminus).

Yeast growth complementation assays. The yeast strains were transformed with each pYTK-e112 plasmid encoding the indicated protein under its endogenous promoter. Cells were selected on SC(−Leu) agar medium. Single colonies were picked and grown overnight in SC(−Leu) medium. The cultures were diluted with water to an optical density of 600 nm (OD₆₀₀) of 1.0 and further serially diluted by factors of 10 (in Fig. 3b,c, starting concentration was OD₆₀₀ = 0.1). The diluted cultures (10 μl each) were spotted on SC(−Leu) agar plates. In the case of Extended Data Fig. 4 (bottom two panels only), YPD agar medium was used. Where indicated, plates contained 10 μg ml⁻¹ of doxycycline. Plates were incubated at 30 °C unless otherwise stated. The following strains were used for the indicated

experiment: TH_5187 (Fig. 3b left panel, Fig. 4 and Extended Data Fig. 8a,b), ySI42 (Fig. 3b right panel), ySI89 (Fig. 3c) and ySI62 (Extended Data Fig. 4c)

Protein purification. For purification of *Sc*Sec complexes, yeast cells (ySI7 for WT, ySI8 for PM, ySI73 for FN3mut, ySI74 for FN3/Δ210–216) were grown in YPD medium to OD$_{600}$ of 2–3, before harvest. For purification of *Tl*Sec, cells were grown in YPD medium to OD$_{600}$ of 1.0. After adding 50 nM β-estradiol, cells were further grown until reaching OD$_{600}$ of 2–3. All cultures were grown in 30 °C, except for the FN3mut/PM and FN3/Δ210–216 variants of *Sc*Sec, for which cells were grown at 22 °C. Cells were harvested by centrifugation (8 min at 6,400g), washed once with ice-cold Tris-buffered saline (20 mM Tris, pH 7.5, and 150 mM NaCl), frozen in liquid nitrogen and stored at −75 °C before use.

All *Sc*Sec and *Tl*Sec complexes were purified as described previously[28]. Briefly, cells were lysed by cryo-milling and resuspended in buffer containing 50 mM Tris, pH 7.5, 200 mM NaCl, 1 mM ethylenediaminetetraacetic acid (EDTA), 10% glycerol, 2 mM dithiothreitol (DTT), 5 μg l⁻¹ of aprotinin, 5 μg l⁻¹ of leupeptin, 1 μg ml⁻¹ of pepstatin A and 1.2 mM phenylmethylsulfonyl fluoride. Membranes were solubilized by adding 1% lauryl maltose neopentyl glycol (Anatrace) and 0.2% cholesteryl hemisuccinate (Anatrace) directly to the whole-cell lysate for 1.5 h at 4 °C. The lysate was clarified by ultracentrifugation at 125,000g for 1 h. The Sec complex was bound to agarose beads conjugated with anti-GFP nanobody and the buffer was exchanged with 50 mM, Tris pH 7.5, 200 mM NaCl, 1.0 mM EDTA, 2 mM DTT, 0.02% glycol-diosgenin (Anatrace) and 10% glycerol. The complex was eluted by incubating the beads with TEV protease (~10 μg ml⁻¹) overnight and further purified by size-exclusion chromatography (Superose 6 Increase, GE Life Sciences) in 20 mM Tris pH 7.5, 100 mM NaCl, 1 mM EDTA, 2 mM DTT and 0.02% glycol-diosgenin. Peak fractions were concentrated to ~5 mg ml⁻¹ and used immediately for cryo-EM. We note that the yields of all mutant *Sc*Sec complexes were comparable to those of the WT complex.

Cryo-EM grid preparation and data collection. Purified samples were supplemented with 3 mM fluorinated Fos-Choline-8 (Anatrace) before plunge freezing. The samples were applied on holey carbon gold grids (Quantifoil 1.2/1.3, 400 mesh) that were glow discharged for 35 s using PELCO easiGlow glow discharge cleaner. Plunge freezing was performed using Vitrobot Mark IV (FEI) set at 4 °C and 100% humidity. Whatman No. 1 filter paper was used to blot the samples.

Datasets for *Tl*Sec, ΔSec62 *Tl*Sec and FN3mut/Δ210–216 *Sc*Sec were collected on an FEI Talos Arctica electron microscope operated at an acceleration voltage of 200 kV. Datasets for WT *Sc*Sec, PM *Sc*Sec, FN3mut *Sc*Sec, FN3mut/PM *Sc*Sec and Δanchor *Tl*Sec were collected on an FEI Titan Krios electron microscope operated at an acceleration voltage of 300 kV and equipped with a Gatan Quantum Image Filter (a slit width of 20 eV). Both microscopes operated using SerialEM software[50]. Videos were recorded on a Gatan K3 Summit direct electron detector under the super-resolution mode (with a physical pixel size of 1.14 Å for *Tl*Sec and ΔSec62 *Tl*Sec, 0.9 Å for FN3mut/Δ210–216 *Sc*Sec, and 1.19 Å for WT *Sc*Sec, FN3mut *Sc*Sec, FN3mut/PM *Sc*Sec and Δanchor *Tl*Sec) with the exception of PM *Sc*Sec, which utilized a Gatan K2 Summit direct election detector (with physical pixel size of 1.15 Å). The samples were exposed to a total dose of ~50 e⁻ per Å² applied over 42 frames. Defocus target was typically set between −0.8 μm and −2.4 μm. For detailed parameters, see also Tables 1 and 2.

Cryo-EM image analysis. Micrographs collected from the microscopes were preprocessed by Warp[51]. Video stacks were corrected for gains and subjected to tile-based motion correction and CTF estimation (7×5 tiles for datasets from the K3 detector and 5×5 for datasets from the K2 detector). Particles were automatically picked using the BoxNet algorithm of Warp. Low-quality micrographs and particles, such as those containing crystalline ice or showing excessive motion blur, were removed by manual inspection. Motion-corrected videos were exported with 2× pixel and 2× frame binning. Local particle motion corrections were performed in cryoSPARC v.2 (ref. [52]) after importing particle metadata and motion-corrected video stacks. Box sizes of extracted particle images were 256 pixels except for the FN3mut/Δ210–216 *Sc*Sec dataset, which was 320 pixels. All subsequent single-particle analyses were performed with cryoSPARC v.2 as described below. In the cases of the WT and FN3mut/Δ210–216 *Sc*Sec datasets, particle images extracted from Warp were directly used without local motion correction.

(1) WT *Sc*Sec: the single-particle analysis procedure for WT *Sc*Sec is outlined in Extended Data Fig. 1b. First, 2,686,839 picked particles were subjected to two-dimensional (2D) classification, where empty micelles and classes of poor quality were removed. Selected 1,679,300 particles were then subjected to reconstruction from scratch to yield three initial models, followed by heterogeneous refinement using the initial maps (unless stated otherwise, particle images were 2× scaled down to 128×128 pixels² in all heterogeneous refinements). Features of the Sec complex appeared in only one class (1,172,728 particles), particles of which were subjected to a second iteration of heterogeneous refinement, with the three classes from the first heterogeneous refinement as references to further remove poor-quality particles. The resulting 995,878 particles were then subjected to a round of

nonuniform refinement, local CTF refinement and another round of nonuniform refinement, yielding a map at 2.98-Å resolution (consensus map). To separate the particles into classes containing and lacking Sec62, the NTD density of Sec62 in the consensus map was manually erased using UCSF Chimera[53] and was used alongside the consensus map as initial references for heterogeneous refinement. This yielded two classes: *Sc*Sec[62−] with 391,885 particles which is largely devoid of detectable Sec62 and *Sc*Sec[62+] with 603,993 particles. After nonuniform refinement, both classes refined to a resolution of 3.07 Å. To further separate into subclasses containing different conformations of Sec62, the particles of *Sc*Sec[Sec62+] were subjected to a round of reconstruction from scratch and heterogeneous refinement to yield five new classes. This step produced two major classes: one lacking Sec71–Sec72 (142,768 particles) and one showing the full complex features (415,818 particles). Particles of the latter class were subjected to a second round of reconstruction from scratch and heterogeneous refinement, yielding five new classes. Of these, two major classes showing the prominent features of the Sec complex (the other three classes did not show clear features of *Sc*Sec) were further refined using nonuniform refinement to yield the final maps of *Sc*Sec[C1] (from 193,263 particles) and *Sc*Sec[C2] (from 193,661 particles) at overall resolutions of 3.16 and 3.14 Å, respectively.

(2) PM *Sc*Sec: the PM *Sc*Sec dataset was analyzed using essentially the same procedure as for WT *Sc*Sec but starting with a dataset of 195,915 auto-picked particles (see Supplementary Fig. 2). After a round of 2D classification, reconstruction from scratch and heterogeneous refinement, the consensus class (91,813 particles) was obtained, which was subjected to nonuniform refinement to yield a 3.53-Å-resolution map. As with WT *Sc*Sec, the particles were further classified to [Sec62−] and [Sec62+] classes by heterogeneous refinement (35,573 and 56,240 particles, respectively), and the structures were refined to maps at resolutions of 4.02 and 3.78 Å, respectively. Particles of the [Sec62+] class were further classified by reconstruction from scratch and heterogeneous refinement (five classes). One class (13,752 particles) lacked the Sec71–72 subunits and the main class (36,506 particles) showed features of the full complex. The particles from the latter class were subjected to another round of reconstruction from scratch and heterogeneous refinement, yielding two main classes, PM *Sc*Sec[C1] (17,341 particles) and PM *Sc*Sec[C2] (16,679 particles), which were further refined with nonuniform refinement to overall resolutions of 4.06 and 4.04 Å, respectively.

(3) FN3mut *Sc*Sec: the single-particle analysis procedure is outlined in Supplementary Fig. 2. The initial set of 1,274,219 auto-picked particles were subjected to 2D classification. After discarding empty micelle classes and classes showing poor features (resulting in 412,129 particles), we generated five initial models with reconstruction from scratch. Only one class showed features of the Sec complex. Particles were subjected to two rounds of heterogeneous refinement to further remove particles of poor quality. The resulting 202,091 particles were used for nonuniform refinement, which was followed by local CTF refinement and a second round of nonuniform refinement to obtain a consensus map at 3.73-Å resolution. Similar to WT *Sc*Sec, these particles were further classified into two classes, one with Sec62 (FN3mut *Sc*Sec[Sec62+], 119,420 particles) and the other without Sec62 (FN3mut *Sc*Sec[Sec62−], 82,671 particles) using the consensus map and Sec62-NTD-erased map as initial references for heterogeneous refinement. FN3mut *Sc*Sec [Sec62+] and [Sec62−] particles were separately subjected to local CTF refinement and nonuniform refinement to yield final maps at 3.90- and 4.01-Å resolution, respectively. Further 3D classification of particles from the [Sec62+] class did not result in classes with a noticeable conformational difference.

(4) FN3mut/PM *Sc*Sec: the single-particle analysis procedure is outlined in Supplementary Fig. 2. The analysis was processed similarly to FN3mut *Sc*Sec. The initial set of 267,541 auto-picked particles was first cleaned up by 2D classification. The resulting 146,399 particles were subjected to reconstruction from scratch (three classes). Only one main class showed features of the Sec complex. The 146,399 particles were then subjected to two rounds of heterogeneous refinement to remove non-Sec-complex particles. The resulting 86,843 particles were then subjected to nonuniform refinement, which was followed by local CTF refinement and a second round of nonuniform refinement to obtain a consensus map at 3.73-Å resolution. The particles were further classified to [Sec62+] and [Sec62−] classes (54,139 and 32,704 particles, respectively) with heterogeneous refinement, and final maps of PM/FN3mut *Sc*Sec [Sec62+] and [Sec62−] at 3.99- and 4.35-Å resolution, respectively, were obtained by nonuniform refinement followed by local CTF refinement and a second round of nonuniform refinement. Further 3D classification of particles from the [Sec62+] class did not yield classes with a noticeable conformational difference.

(5) FN3mut/Δ210–216 *Sc*Sec: the single-particle analysis procedure is outlined in Extended Data Fig. 10d. The initial set of 2,270,392 auto-picked particles were cleaned up by 2D classification. The resulting 646,998 particles were used to generate four initial maps with reconstruction from scratch. Only one main class showed features of the Sec complex. Two rounds of heterogeneous refinement (with particle image 2× scaled down to 160×160 pixels²) were performed to enrich particles of the Sec complex. The resulting 282,555

particles were subjected to nonuniform refinement, followed by local CTF refinement and a second round of nonuniform refinement to produce a 3.80-Å resolution map. The particles were then subjected to a second round of reconstruction from scratch and heterogeneous refinement to generate four classes. Of these classes, two showed features of the Sec complex (131,010 and 126,221 particles), maps of which were nearly identical. Particles of the two classes were combined for nonuniform refinement to yield the final map at 3.75-Å resolution.

(6) WT *Tl*Sec: the single-particle analysis procedure is outlined in Extended Data Fig. 2b. The initial set of 1,632,719 auto-picked particles was subjected to 2D classification in two batches to remove empty micelles and poor-quality particles. The resulting 789,004 particles were used to generate five initial 3D maps with reconstruction from scratch. Only one (main) class showed features of the Sec complex. The 789,004 particles were subjected to heterogeneous refinement using the initial maps as references, which was followed by a second round of heterogeneous refinement. The resulting main class (427,835 particles) was refined using nonuniform refinement, local CTF refinement and a second nonuniform refinement, yielding a consensus map at 3.61-Å resolution. As with WT *Sc*Sec, particles were further classified to [Sec62+] and [Sec62−] classes with heterogeneous refinement using the consensus map and a Sec62-NTD-erased map as references (272,224 and 155,601 particles, respectively). The classes were further refined with nonuniform refinement yielding a 3.88-Å-resolution map of *Tl*Sec[Sec62−] and a 3.75-Å-resolution map of *Tl*Sec[Sec62+]. Particles of the [Sec62+] class (272,224 particles) were further subjected to reconstruction from scratch and heterogeneous refinement (five classes). Two major classes (114,704 and 143,227 particles) showed the features of the Sec complex, which were further refined to the final maps of [Sec62+/plug-open] and [Sec62+/plug-closed] at overall resolutions of 4.02 and 3.76 Å, respectively. Unlike WT *Sc*Sec, a class lacking Sec71-ec72 was not identified.

(7) ΔSec62 *Tl*Sec: the single-particle analysis procedure is outlined in Supplementary Fig. 2. The initial set of 546,712 auto-picked particles was subjected to two rounds of 2D classification with removal of poor classes in each round, resulting in 258,743 particles. Five initial 3D models were generated from the 258,743 selected particles by reconstruction from scratch and further refined by heterogeneous refinement. This produced two major classes (77,524 and 114,523 particles) which showed features of the Sec complex. Particles from the two classes were combined and refined with nonuniform refinement, local CTF refinement and a second nonuniform refinement, yielding the final map at 3.74-Å overall resolution.

(8) Δanchor *Tl*Sec: the initial set of 229,825 auto-picked particles was subjected to 2D classification, resulting in 105,578 particles. Three initial 3D models were generated by reconstruction from scratch and refined by heterogeneous refinement. One major class (76,726 particles) showed features of the Sec complex, and the particles from this class were used to generate the final map at 4.38-Å resolution with nonuniform refinement.

For additional Fourier shell correlation curves between the two half-maps of final reconstructions, particle orientation distributions and local resolution distributions, see Supplementary Figs. 3–5.

Atomic model building. Atomic models were built using Coot[54]. We first built models for *Sc*Sec[Sec62−] and ΔSec62 *Tl*Sec using our previous *Sc*Sec model (PDB 6N3Q)[28] as a template. For ΔSec62 *Tl*Sec, we generated a homology model using SWISS-MODEL[55], which was rebuilt into the map using Coot. The *Sc*Sec[Sec62−] model was then used to build models for *Sc*Sec[C1] and *Sc*Sec[C2]. For *Sc*Sec62, a poly(alanine) model was built into densities. Atomic models for all the mutant *Sc*Sec structures lacking Sec62 were also built starting from the *Sc*Sec[Sec62−] model. The *Sc*Sec[Sec62−] model was first fitted into each map using UCSF Chimera and further fitted into the map in groups of domains and subunits using rigid body refinement in Phenix[56]. The models were then locally adjusted in Coot. Models for PM *Sc*Sec[C1] and PM *Sc*Sec[C2] were built similarly using the WT *Sc*Sec[C1] and *Sc*Sec[C2] models as starting models. Models for FN3mut *Sc*Sec[Sec62+] and PM/FN3mut *Sc*Sec[Sec62+] were built starting with the WT *Sc*Sec[C2] and PM/FN3mut *Sc*Sec[Sec62−] model, respectively. ΔSec62 *Tl*Sec was used as a starting model to build all *Tl*Sec structures.

The models were refined with Phenix real-space refinement using combined maps that were sharpened with a B factor estimate based on the Guinier plot and low pass filtered at their overall resolution (produced by cryoSPARC). The refinement resolution was also limited to the overall resolution of the maps in Phenix. Secondary structure restraints were used during the refinement. MolProbity[57] was used for structural validation. For refinement and validation statistics, see Tables 1 and 2.

UCSF Chimera[53], ChimeraX[58] and PyMOL (Schrödinger) were used to prepare figures in the article. Unless stated otherwise, all shown cryo-EM maps are unsharpened maps that were low pass filtered at their overall resolution.

MD simulations. Protein models of *Sc*Sec[C1], *Sc*Sec[C2], *Sc*Sec[Sec62−], WT *Tl*Sec and ΔSec62 *Tl*Sec suitable for MD simulation were built from the cryo-EM-derived atomic models. Missing areas of the overall complexes were modeled in using SWISS-MODEL[55], although omitting the unstructured region of *Tl*Sec63, residues 482–526. The sequence of the TM portion of Sec62 was mapped on to the structure; gaps in the structures of other proteins were modeled except for the J domain of Sec63. MD flexible fitting[59] was used to fit the newly modeled pieces of the structures to optimize their positions within the density maps, including the Sec61 plug. All five systems were placed in a realistic yeast ER membrane with 47% POPC, 20% POPE, 10% PLPI, 8% POPS, 3% POPA, 10% ERG, 1% TLCL and 1% DYGL[60,61] using CHARMM-GUI[62,63]. The membrane protein systems were placed in a TIP3 (ref. [64]) water box and neutralized with 0.15 M KCl. The all-atom systems ranged from 250,000 to 270,000 atoms in size.

All simulations were run using NAMD 2.14 (ref. [65]) with the CHARMM36m (protein)[66,67] and CHARMM36 (lipid)[68] force fields as well as hydrogen mass repartitioning[69]. Positional restraints were initially placed on all atoms in each system and were gradually released in two consecutive runs: 0.5 ns with only the lipid tails unrestrained and 1 ns with the protein restrained. Subsequent 200-ns runs maintained restraints on the protein backbone to focus on the behavior of lipids for a given conformation of the Sec complex. All simulations were performed at a constant temperature of 310 K using Langevin dynamics (damping coefficient 1/ps), a constant pressure of 1 atm using Langevin piston and periodic boundary conditions. As hydrogen mass repartitioning was used, the time step was set to 4 fs. Short-range, nonbonded interactions were cut off at 12 Å, with a force-based switching function starting at 11 Å. Long-range, nonbonded interactions were calculated using a particle-mesh Ewald method with grid spacing of at least $1/Å^3$ (ref. [70]). Total simulation time between all systems was 1.4 µs. Setup, analysis and visualization were carried out using visual molecular dynamics[71].

Reporting summary. Further information on research design is available in the Nature Research Reporting Summary linked to this article.

Data availability

The atomic coordinates and cryo-EM density maps of the Sec complexes have been deposited to the Protein Data Bank (wwPDB) and Electron Microscopy Data Bank (EMDB), respectively. Their PDB and EMDB accession codes are as follows: EMD-22785 for *Sc*Sec[consensus]; PDB 7KAH and EMD-22770 for *Sc*Sec[Sec62−]; PDB 7KAI and EMD-22771 for *Sc*Sec[C1]; PDB 7KAJ and EMD-22772 for *Sc*Sec[C2]; PDB 7KAO and EMD-22778 for PM *Sc*Sec[Sec62−]; PDB 7KAP and EMD-22779 for PM *Sc*Sec[C1]; PDB 7KAQ and EMD-22780 for PM *Sc*Sec[C2]; PDB 7KAR and EMD-22781 for FN3mut *Sc*Sec[Sec62−]; PDB 7KAS and EMD-22782 for FN3mut *Sc*Sec[Sec62+]; PDB 7KAT and EMD-22783 for PM/FN3mut *Sc*Sec[Sec62−]; PDB 7KAU and EMD-22784 for PM/FN3mut *Sc*Sec[Sec62+]; PDB 7KB5 and EMD-22787 for FN3mut/Δ210–216 *Sc*Sec; EMD-22786 for WT *Tl*Sec[Sec62+]; PDB 7KAK and EMD-22773 for *Tl*Sec[Sec62−]; PDB 7KAL and EMD-22774 for *Tl*Sec[Sec62+/plug-open]; PDB 7KAM and EMD-22775 for *Tl*Sec[Sec62+/plug-closed]; PDB 7KAN and EMD-22776 for ΔSec62 *Tl*Sec; EMD-22777 for Δanchor *Tl*Sec. Source data are provided with this paper.

References

46. Hughes, T. R. et al. Functional discovery via a compendium of expression profiles. *Cell* **102**, 109–126 (2000).
47. Hentges, P., Van Driessche, B., Tafforeau, L., Vandenhaute, J. & Carr, A. M. Three novel antibiotic marker cassettes for gene disruption and marker switching in *Schizosaccharomyces pombe*. *Yeast* **22**, 1013–1019 (2005).
48. McIsaac, R. S. et al. Fast-acting and nearly gratuitous induction of gene expression and protein depletion in *Saccharomyces cerevisiae*. *Mol. Biol. Cell* **22**, 4447–4459 (2011).
49. Lee, M. E., DeLoache, W. C., Cervantes, B. & Dueber, J. E. A highly characterized yeast toolkit for modular, multipart assembly. *ACS Synth. Biol.* **4**, 975–986 (2015).
50. Mastronarde, D. N. Automated electron microscope tomography using robust prediction of specimen movements. *J. Struct. Biol.* **152**, 36–51 (2005).
51. Tegunov, D. & Cramer, P. Real-time cryo-electron microscopy data preprocessing with Warp. *Nat. Methods* **16**, 1146–1152 (2019).
52. Punjani, A., Rubinstein, J. L., Fleet, D. J. & Brubaker, M. A. cryoSPARC: algorithms for rapid unsupervised cryo-EM structure determination. *Nat. Methods* **14**, 290–296 (2017).
53. Pettersen, E. F. et al. UCSF Chimera—a visualization system for exploratory research and analysis. *J. Comput. Chem.* **25**, 1605–1612 (2004).
54. Emsley, P., Lohkamp, B., Scott, W. G. & Cowtan, K. Features and development of *Coot*. *Acta Crystallogr. D Biol. Crystallogr.* **66**, 486–501 (2010).
55. Waterhouse, A. et al. SWISS-MODEL: homology modelling of protein structures and complexes. *Nucleic Acids Res.* **46**, W296–W303 (2018).
56. Afonine, P. V. et al. Real-space refinement in *PHENIX* for cryo-EM and crystallography. *Acta Crystallogr. D Struct. Biol.* **74**, 531–544 (2018).
57. Chen, V. B. et al. *MolProbity*: all-atom structure validation for macromolecular crystallography. *Acta Crystallogr. D Biol. Crystallogr.* **66**, 12–21 (2010).

58. Goddard, T. D. et al. UCSF ChimeraX: meeting modern challenges in visualization and analysis. *Protein Sci.* **27**, 14–25 (2018).
59. Trabuco, L. G., Villa, E., Mitra, K., Frank, J. & Schulten, K. Flexible fitting of atomic structures into electron microscopy maps using molecular dynamics. *Structure* **16**, 673–683 (2008).
60. Sugiura, S. & Mima, J. Physiological lipid composition is vital for homotypic ER membrane fusion mediated by the dynamin-related GTPase Sey1p. *Sci. Rep.* **6**, 20407 (2016).
61. Ganesan, S., Shabits, B. N. & Zaremberg, V. Tracking diacylglycerol and phosphatidic acid pools in budding yeast. *Lipid Insights* **8**, 75–85 (2015).
62. Jo, S., Kim, T., Iyer, V. G. & Im, W. CHARMM-GUI: a web-based graphical user interface for CHARMM. *J. Comput. Chem.* **29**, 1859–1865 (2008).
63. Wu, E. L. et al. CHARMM-GUI membrane builder toward realistic biological membrane simulations. *J. Comput. Chem.* **35**, 1997–2004 (2014).
64. Jorgensen, W. L., Chandrasekhar, J., Madura, J. D., Impey, R. W. & Klein, M. L. Comparison of simple potential functions for simulating liquid water. *J. Chem. Phys.* **79**, 926–935 (1983).
65. Phillips, J. C. et al. Scalable molecular dynamics with NAMD. *J. Comput. Chem.* **26**, 1781–1802 (2005).
66. Best, R. B. et al. Optimization of the additive CHARMM all-atom protein force field targeting improved sampling of the backbone φ, ψ and side-chain χ_1 and χ_2 dihedral angles. *J. Chem. Theory Comput.* **8**, 3257–3273 (2012).
67. Huang, J. et al. CHARMM36m: an improved force field for folded and intrinsically disordered proteins. *Nat. Methods* **14**, 71–73 (2017).
68. Klauda, J. B. et al. Update of the CHARMM all-atom additive force field for lipids: validation on six lipid types. *J. Phys. Chem. B* **114**, 7830–7843 (2010).
69. Balusek, C. et al. Accelerating membrane simulations with hydrogen mass repartitioning. *J. Chem. Theory Comput.* **15**, 4673–4686 (2019).
70. Darden, T., York, D. & Pedersen, L. Particle mesh Ewald—an $N \cdot \log(N)$ method for Ewald sums in large systems. *J. Chem. Phys.* **98**, 10089–10092 (1993).
71. Humphrey, W., Dalke, A. & Schulten, K. VMD: visual molecular dynamics. *J. Mol. Graph Model* **14**, 33–38 (1996).

Author contributions

S.I. prepared samples and performed functional analysis. S.I. and E.P. collected and analyzed cryo-EM data, built atomic models and interpreted the results. K.M.K and J.C.G performed MD simulations and interpreted the results. E.P. supervised the project and wrote the manuscript with input from all the authors.

Competing interests

The authors declare no competing interests.

Additional information

Extended data is available for this paper at https://doi.org/10.1038/s41594-020-00541-x.

Supplementary information is available for this paper at https://doi.org/10.1038/s41594-020-00541-x.

Correspondence and requests for materials should be addressed to E.P.

Peer review information *Nature Structural & Molecular Biology* thanks Ian Collinson and Friedrich Förster for their contribution to the peer review of this work. Peer reviewer reports are available. Anke Sparmann was the primary editor on this article and managed its editorial process and peer review in collaboration with the rest of the editorial team.

**Reprints and permissions information** is available at www.nature.com/reprints.
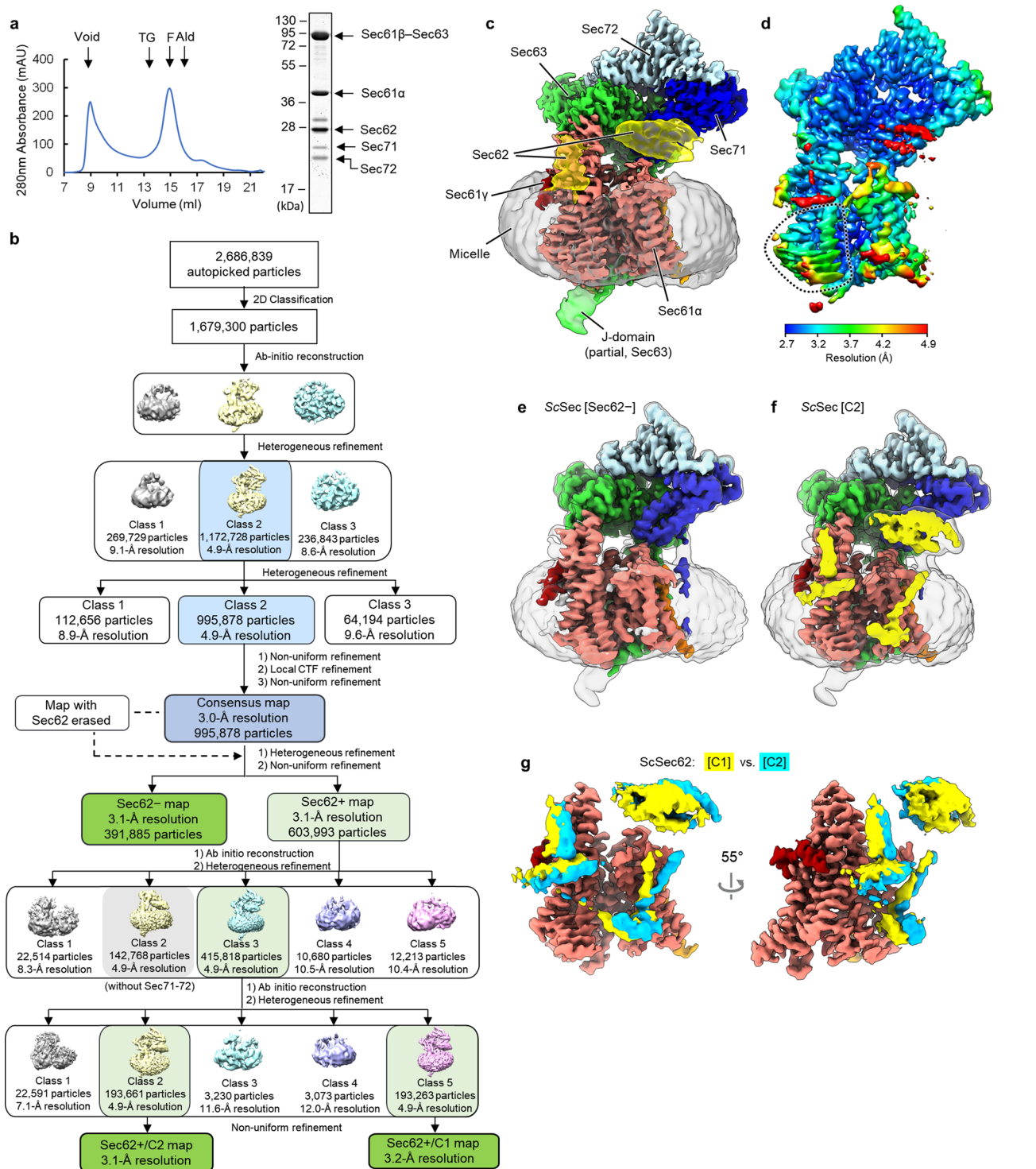
Extended Data Fig. 1 | Cryo-EM analysis of the wild-type (WT) *S. cerevisiae* Sec complex (*Sc*Sec). a, Purification of the WT *Sc*Sec complex. Left, a chromatogram from Superose 6 size-exclusion chromatography of the affinity purified WT *Sc*Sec complex (MW standards: Tg, thyroglobulin; F, ferritin; Ald, aldolase). Right, the Coomassie-stained SDS-PAGE gel of the Superose 6 peak fraction. In this gel, Sec61γ (~10 kDa) migrated off the bottom. **b**, A diagram of the cryo-EM single particle analysis procedure. **c**, The 3.0-Å-resolution consensus map of *Sc*Sec. Salmon, Sec61α; orange, Sec61β; red, Sec61γ; yellow, Sec62; green, Sec63; blue, Sec71; light blue, Sec72; Grey, detergent micelle. Semitransparent surface, lowpass-filtered (5 Å for Sec62 and the J-domain and 7 Å for the micelle) maps shown at a lower contour level. **d**, As in c, but showing a local resolution map. Note that in addition to Sec62, the TM7–TM8 region of Sec61α (dotted line) displays noticeably lower solution than the overall resolution due to conformational heterogeneity (see Fig. 2a). **e**, As in c, but with the 3.1-Å-resolution map of the Sec62− class. Semitransparent surface, 6-Å-lowpass-filtered map at a lower contour level. **f**, As in c, but with the 3.1-Å-resolution map of the Sec62+/C2 class. **g**, The Sec62 densities of the C1 (yellow) and C2 (cyan) classes were compared after aligning the two cryo-EM maps. For simplicity, only Sec61 (from the C1 class) and Sec62 are shown. An uncropped image for panel a is available as source data.
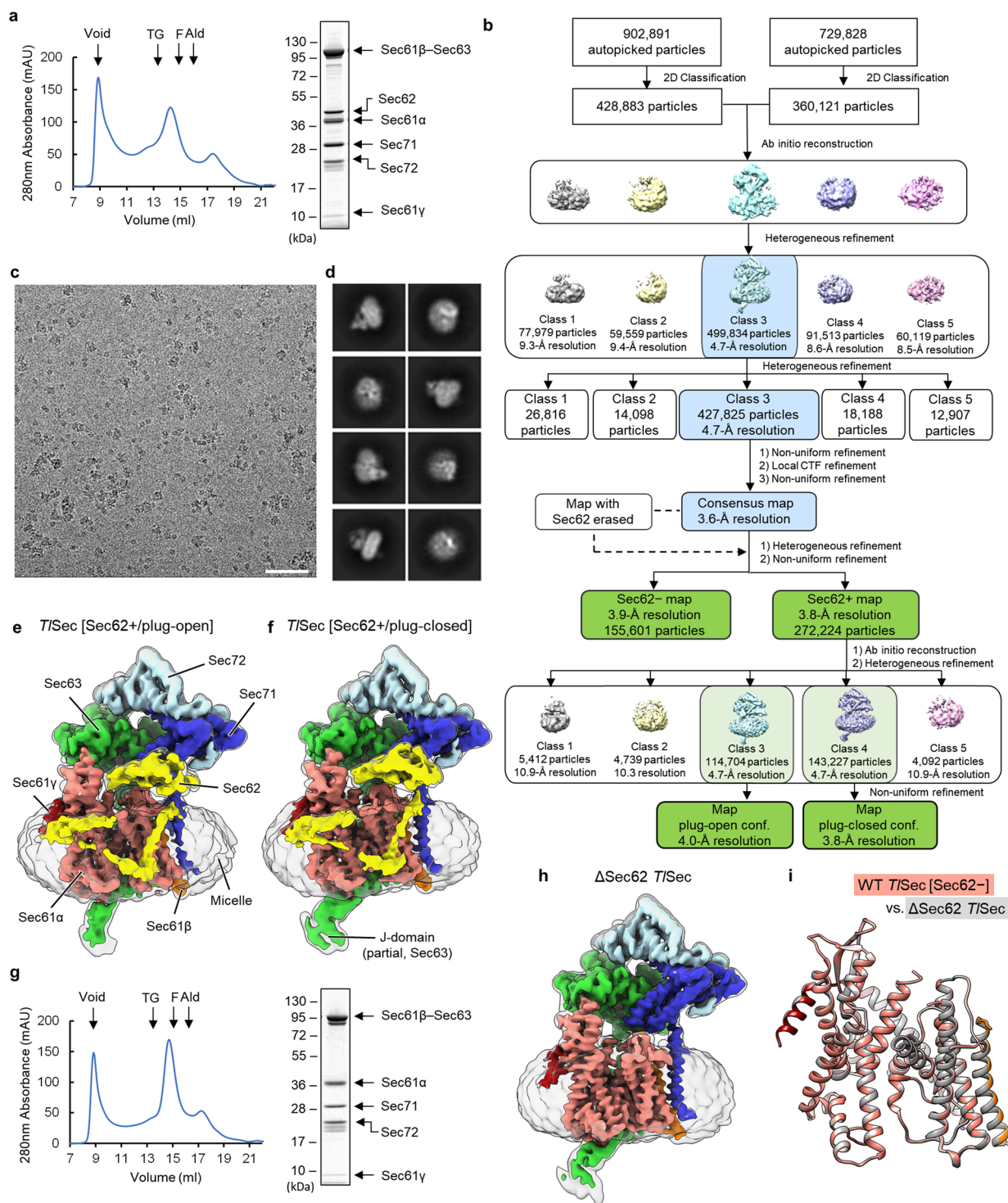
Extended Data Fig. 2 | Cryo-EM analysis of the WT and ΔSec62 *T. lanuginosus* Sec complexes (*Tl*Sec). a, Purification of the WT *Tl*Sec complex. Left, a chromatogram from Superose 6 size-exclusion chromatography of the affinity purified WT *Tl*Sec complex. Right, the Coomassie-stained SDS-PAGE gel of the Superose 6 peak fraction. **b**, A diagram of the cryo-EM single particle analysis procedure. **c**, A representative cryo-EM micrograph. Scale bar, 50 nm. **d**, Examples of selected 2D class averages. **e**, The 4.0-Å-resolution map of the Sec62+/plug-open class of WT *Tl*Sec. The color scheme is the same as in Fig. 1. Semitransparent surface, a 7-Å-lowpass-filtered map shown at a lower contour level. **f**, As in e, but showing the 3.8-Å-resolution map of the Sec62+/plug-closed class. **g**, As in a, but purification of the ΔSec62 *Tl*Sec complex. **h**, As in e, but with the 3.7-Å-resolution map of ΔSec62 *Tl*Sec complex. **i**, The atomic models of the Sec61 complexes from the Sec62− class of WT *Tl*Sec (in color) and the ΔSec62 *Tl*Sec structure (in grey) were aligned and compared (RMSD of Cα atoms is 0.24Å). Uncropped images for panels a and g are available as source data.
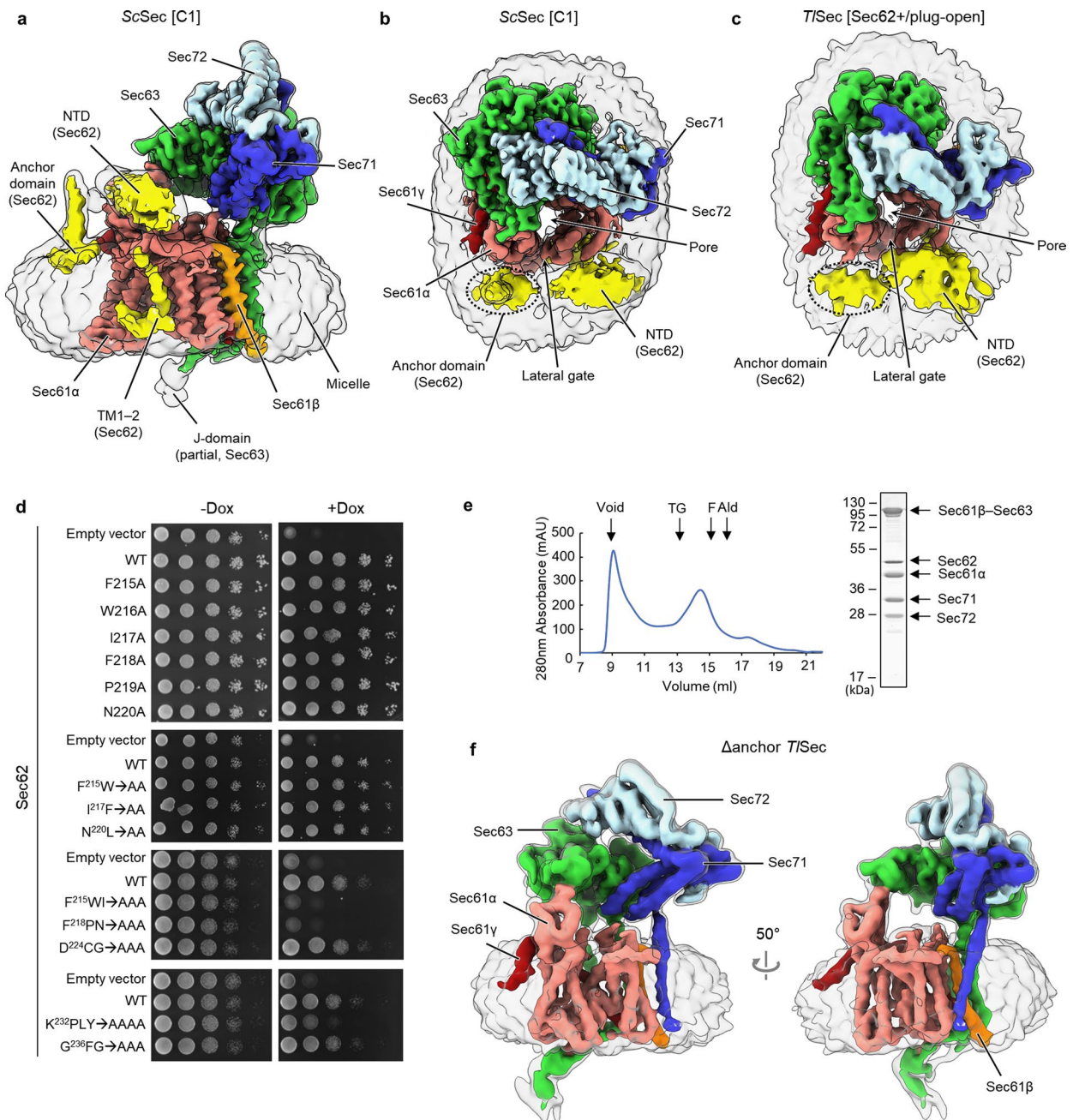
Extended Data Fig. 3 | Structure and mutagenesis analysis of the anchor domain of Sec62. a, As in Fig. 1a, but a side view additionally showing a 6-Å-lowpass-filtered map at a lower contour level (semitransparent surface). **b**, As in a, but showing a view from cytosol. The anchor domain of Sec62 is indicated by a dotted oval. **c**, As in b, but showing the map of the Sec62+/plug-open class of *Tl*Sec. Semitransparent surface is a 7-Å-lowpass-filtered map. **d**, Yeast growth complementation tests for Sec62 anchor mutants. The yeast strain (ySI62) whose endogenous Sec62 is expressed under a tetracycline-repressible promoter was transformed with a CEN/ARS plasmid expressing WT or indicated mutant Sec62 under its native promoter. As a control, empty vector was used. In the right panels, 10 μg/mL doxycycline was included to repress the expression of endogenous Sec62. All growth assays were performed at 30 °C. The top two panels (single and double mutants) were grown on synthetic complete (SC) medium lacking leucine, and the bottom two panels (triple and quadruple Ala mutants) were grown on YPD medium. **e**, As in Extended Data Fig 2a, but with the Δanchor mutant of *Tl*Sec. **f**, As in Extended Data Fig. 2e, but showing the 4.4-Å-resolution map of Δanchor *Tl*Sec. Semitransparent surface, 7-Å-lowpass-filtered map at a lower contour level. We note that the conformation of Δanchor *Tl*Sec is essentially identical to ΔSec62 *Tl*Sec. An uncropped image for panel e is available as source data.
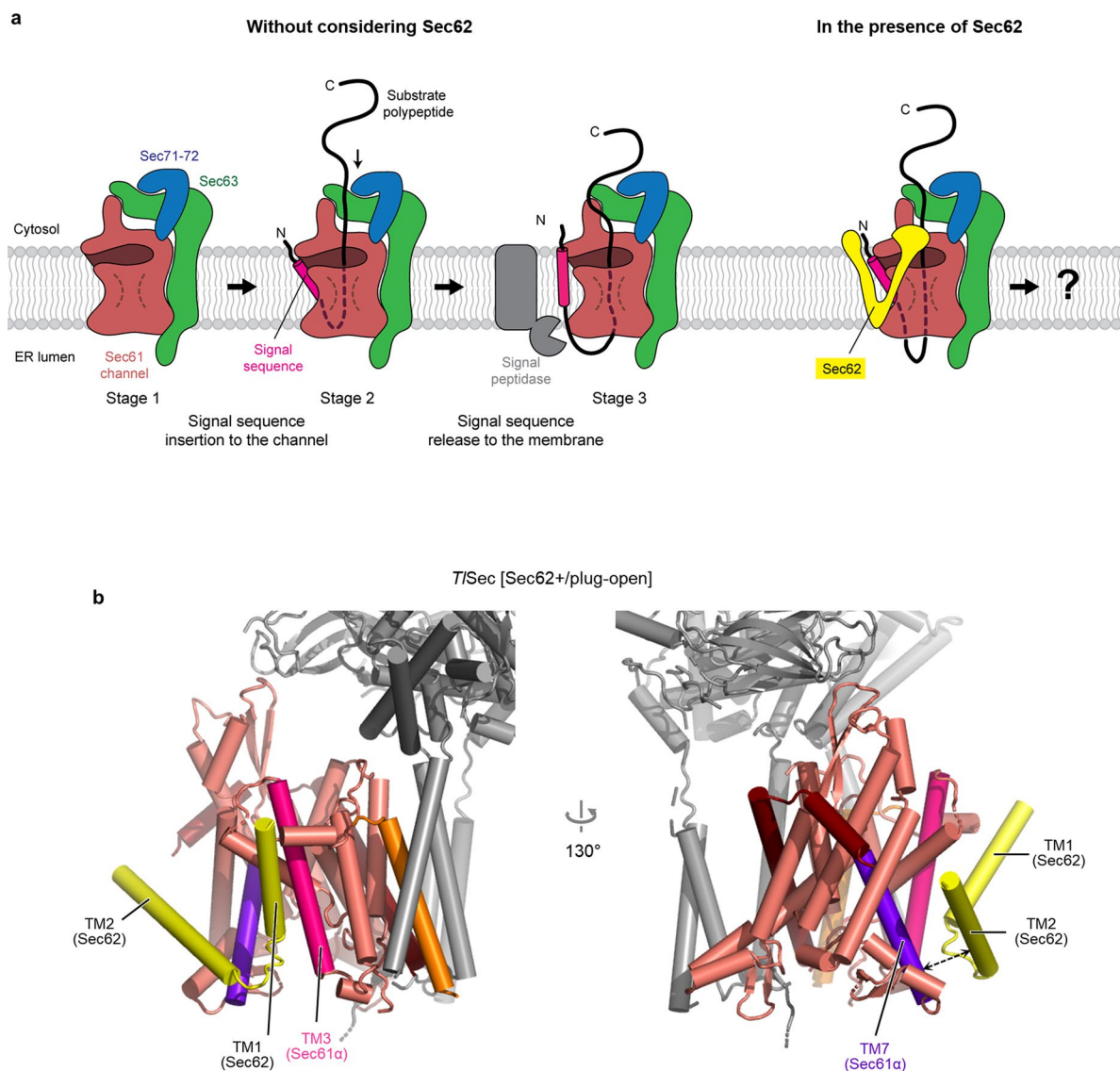
Extended Data Fig. 4 | A potential path for signal sequence release from the lateral gate into the membrane. a, Schematic model for substrate insertion into the Sec complex and translocation. Substrates are expected to insert into the Sec61 channel as a loop with both N- and C-termini exposed in the cytosol. The N-terminal signal sequence may sit at the lateral gate (Stage 2) as seen in the structures of eukaryotic co-translational and bacterial post-translational translocation intermediates[10-12]. In a later stage, the signal sequence is cleavage by the signal peptidase. Although the exact timing remains unclear, one likely scenario is that the signal sequence needs to be released into the membrane prior to cleavage. Alternatively, the signal sequence may be cleaved by the signal peptidase while it is sitting at the lateral gate. In the former case, the presence of Sec62 may cause the signal sequence to be trapped at the lateral gate if Sec62 forms tight contacts with the lateral gate (right). In the latter scenario, signal sequence cleavage may be inhibited due to reduced accessibility of the cleavage site for the signal peptidase. **b**, As in Fig. 1e, but with the *Tl*Sec[Sec62+/plug-down] structure. Dashed arrow, a gap between TM2 of Sec62 and TM7 of Sec61α.
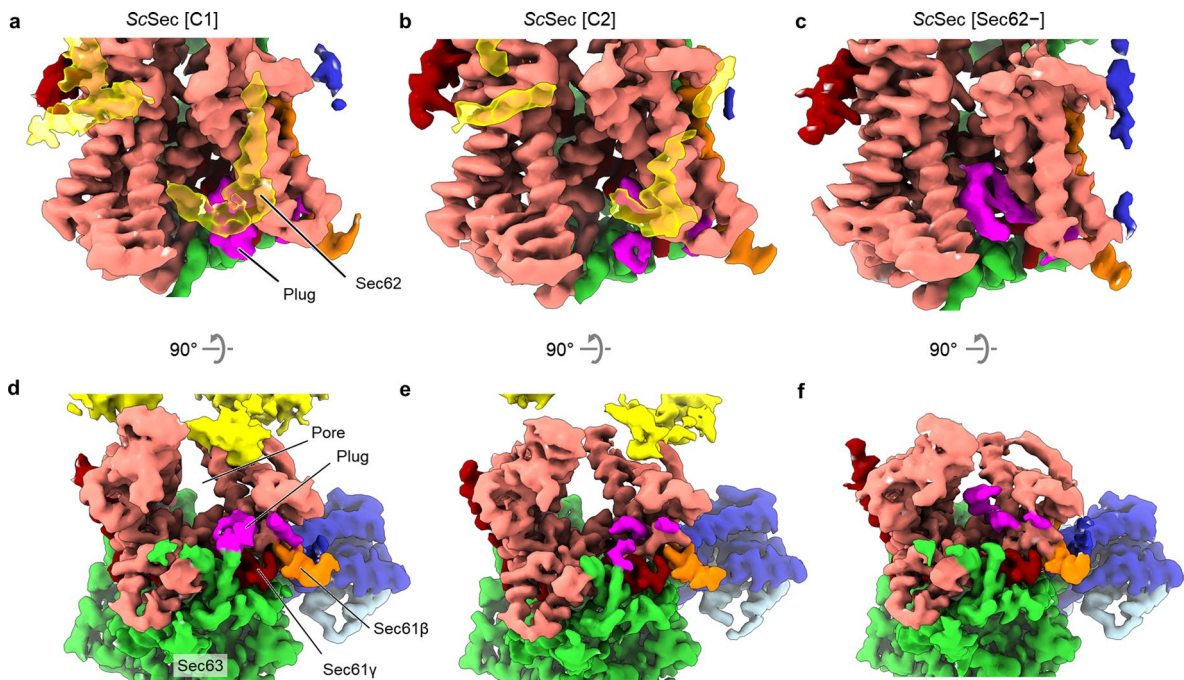
Extended Data Fig. 5 | The presence of Sec62 induces opening of the vertical gate of Sec61 by displacing the plug domain from the closed position.
a–**c**, Views into the lateral gate (front view) of the three classes of the WT *Sc*Sec structure, C1, C2, and Sec62−. Color scheme: salmon, Sec61α; orange, Sec61β; red, Sec61γ; yellow, Sec62; green, Sec63; blue, Sec71; light blue, Sec72; magenta, the plug domain. **d**–**f**, as in a–c, but showing views from the ER lumen.
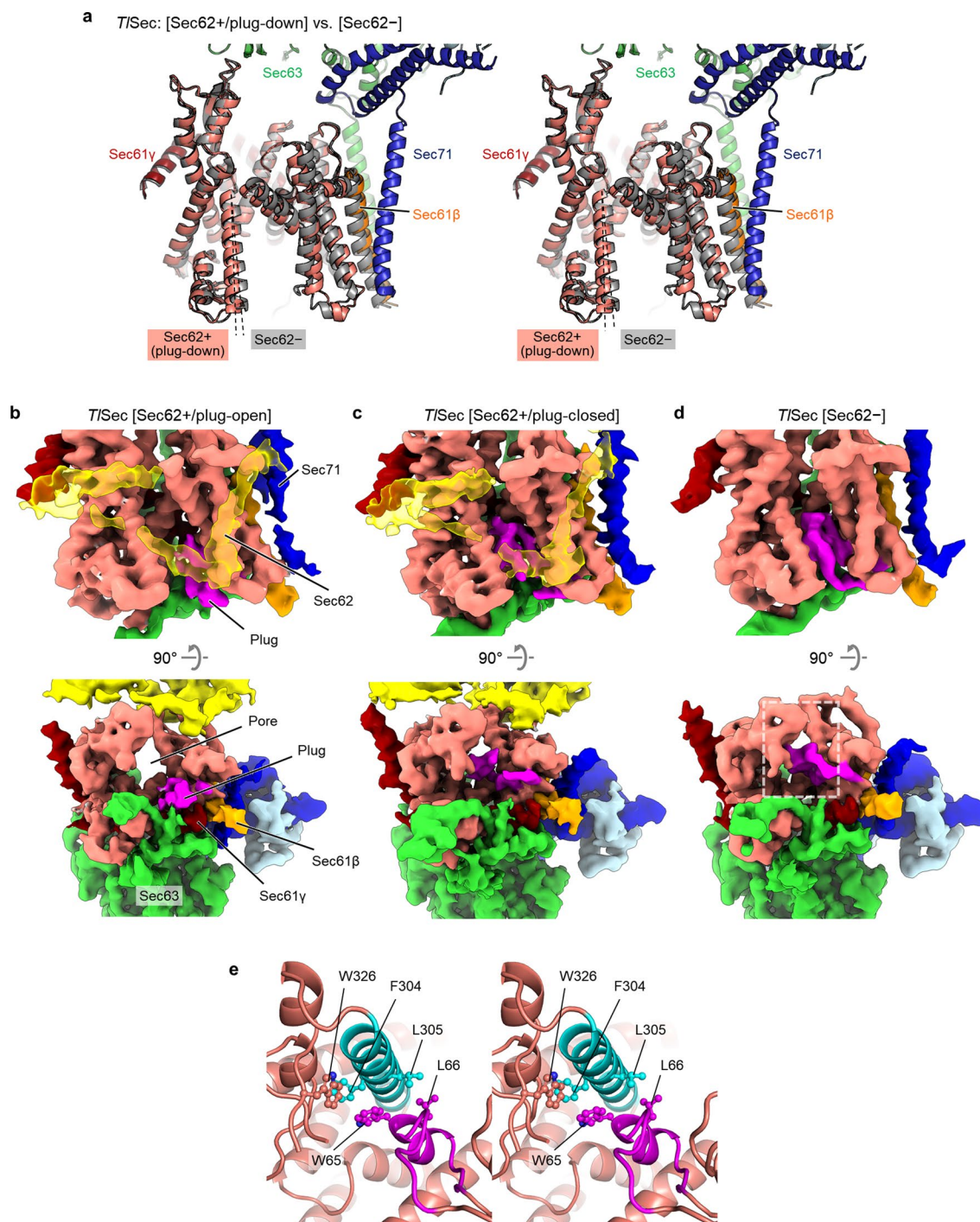
Extended Data Fig. 6 | Conformational changes in the lateral gate and plug domain by Sec62 in the *Tl*Sec complex. a, As in Fig. 2a, but with the WT *Tl*Sec (stereo view). Two classes, Sec62+/plug-open (in color) and Sec62− (grey) are shown. Dashed line, TM7 of Sec61α. For simplicity, Sec62 and the plug are not shown. We note that in the Sec62+/plug-closed class, TM7 assumes an intermediate position of the plug-open and Sec62− classes. **b**–**d**, As in Extended Data Fig. 6 but with the WT *Tl*Sec structures. Shows are front views (upper panels) and views from the ER lumen (lower panels). We note that in both the plug-open and plug-closed classes, the conformation of Sec62 (yellow) is similar to that of the *Sc*Sec[C2] structure. The area indicated by a white dashed box in g are shown in e. **e**, A stereo view showing an interaction between the plug domain (magenta) and TM7 (cyan) of Sec61α. Side chains that are involved in the interaction are shown in a ball and stick representation. W326 belongs to the loop 7/8 of Sec61α. Shown is the ΔSec62 *Tl*Sec structure. We note that a highly similar interaction is also present in the crystal structure of *P. furiosus* SecY (ref. 33; PDB ID 3MP7).
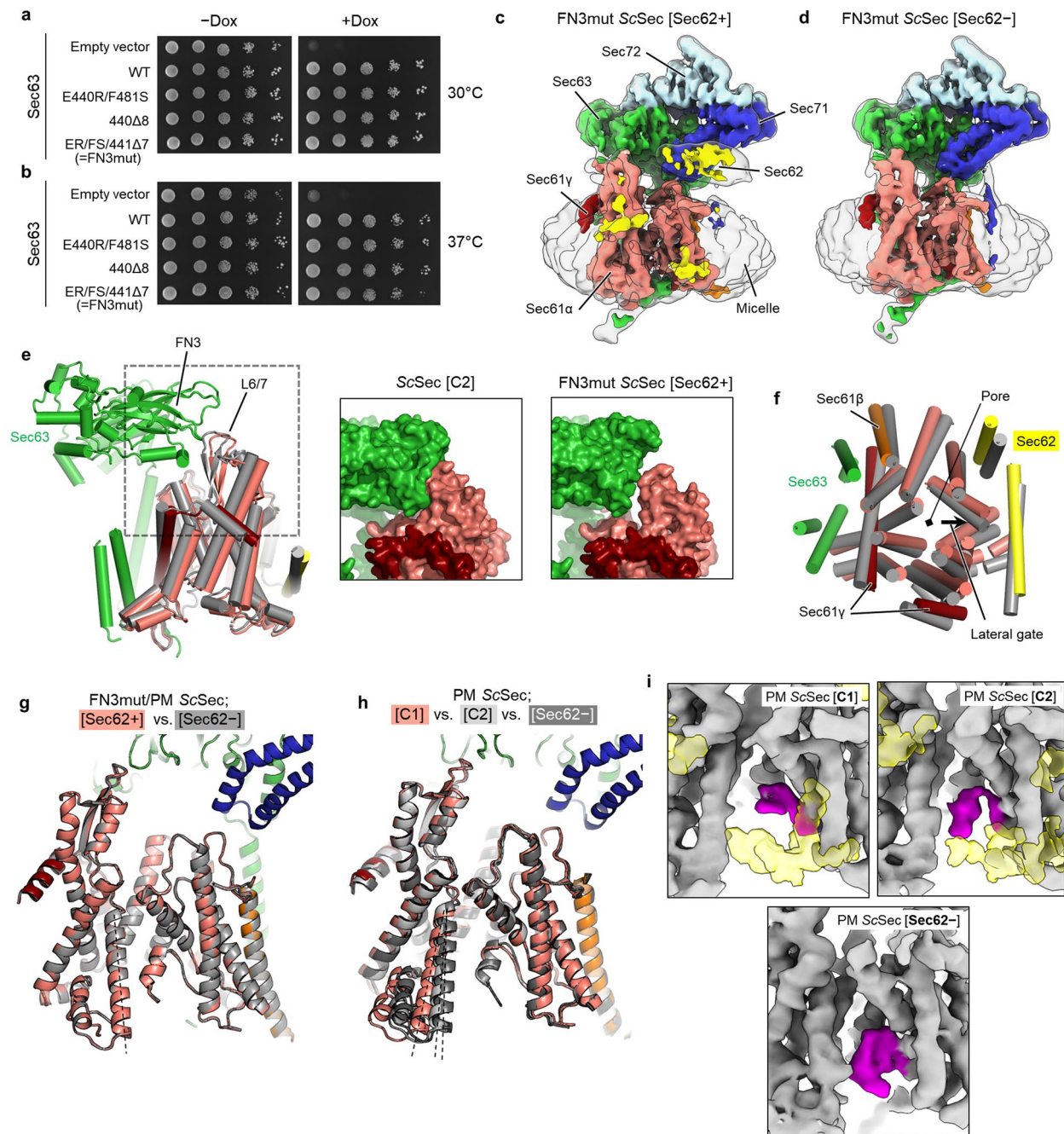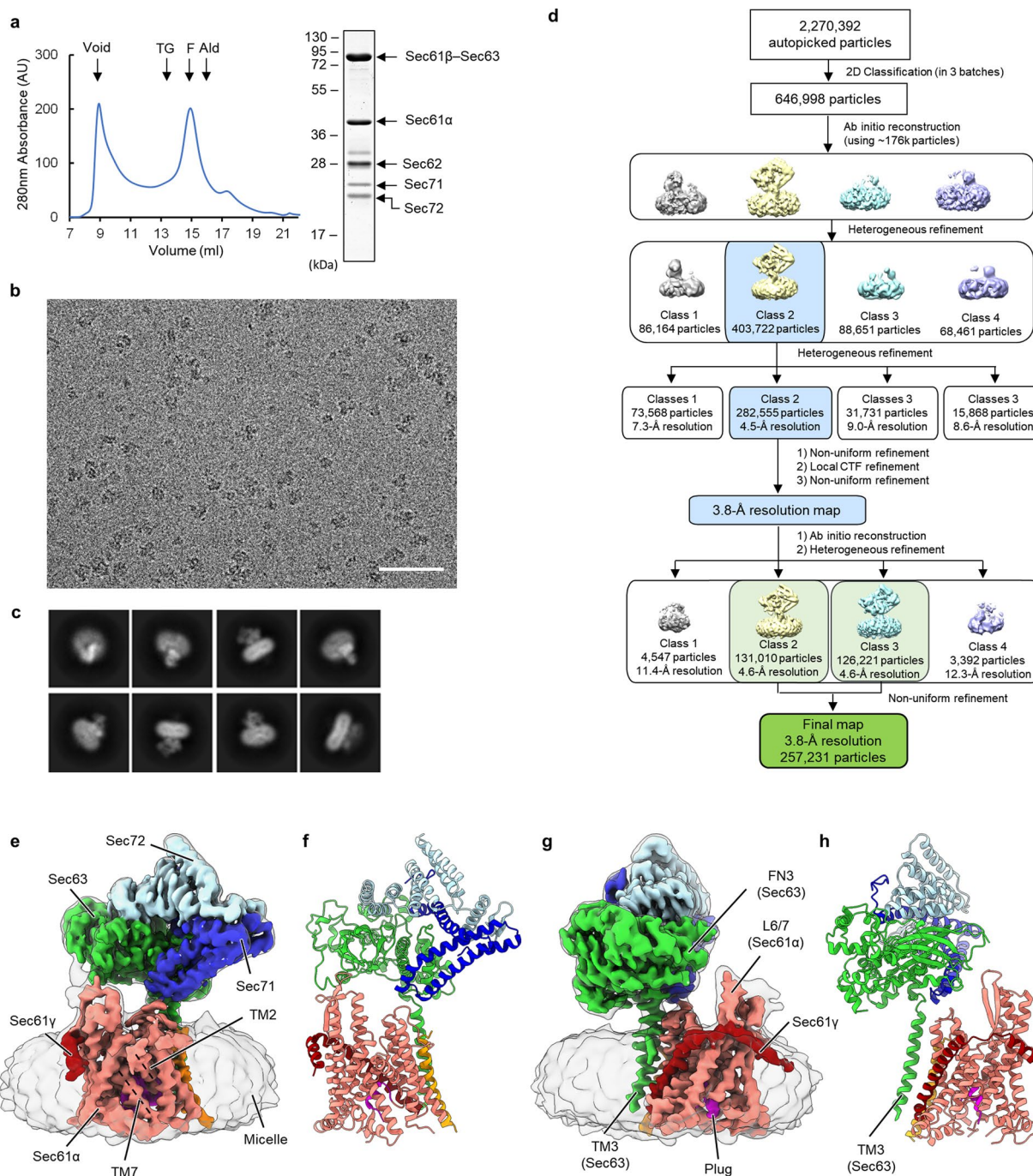
Extended Data Fig. 7 | Structures of the *Sc*Sec complex containing mutations in the FN3 domain of Sec62 and the pore ring of Sec61α. a, The same yeast growth complementation experiment shown in Fig. 3b (left panel), but additionally showing a control without doxycycline. The experiments were repeated three times with similar results. **b**, As in a, but the plates were incubated at 37 °C. **c**, The 3.9-Å-resolution cryo-EM map of the Sec62+ class of the FN3mut *Sc*Sec complex. **d**, As in c, but with the 4.0-Å-resolution cryo-EM map of the Sec62− class of the FN3mut *Sc*Sec complex. **e**, The interaction between the FN3 domain of Sec63 and the L6/7 of Sec61α. Left, a side view showing Sec63 (green) and the Sec61 complex (grey, C2 class of WT *Sc*Sec; color, Sec62+ class of FN3mut *Sc*Sec). The structures were aligned with respect to Sec63. The area indicated by a grey dashed box is shown in the middle and right panels with a solvent-accessible surface representation. **f**, As in the left panel of e, but showing the cytosolic view into the Sec61 complex. **g**, As in Fig. 2a, but comparing the Sec62+ and Sec62− classes of FN3mut/PM *Sc*Sec. **h**, As in Fig. 2a, but comparing the three classes of PM *Sc*Sec. **i**, As in Fig. 3e, but with PM *Sc*Sec. We note that although the plug domain is partly visible in the C1 and C2 classes of PM *Sc*Sec, its density is substantially weaker than that of the Sec62− class.
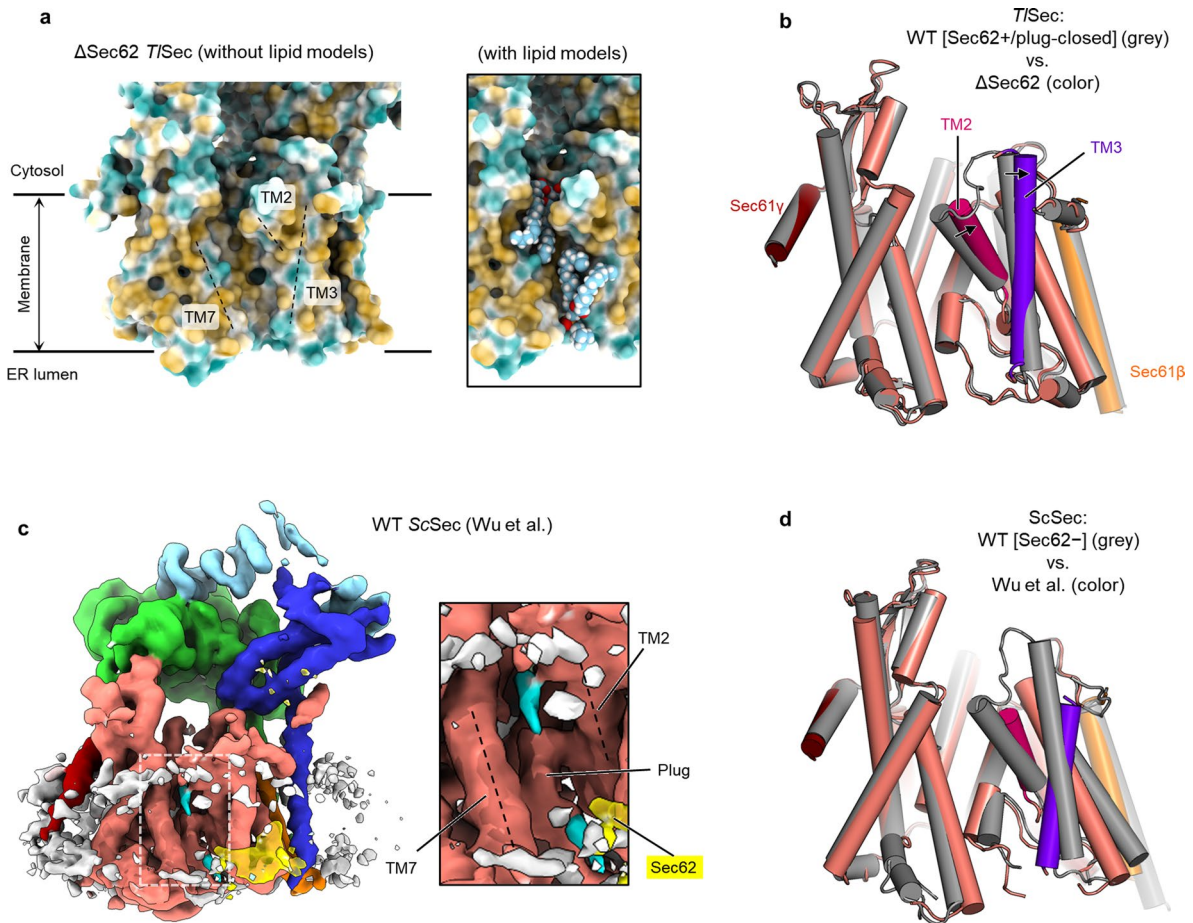
Extended Data Fig. 8 | Lipid/detergent molecules at the lateral gate. a, A view into the lateral gate of the Sec61 channel in ΔSec62 *Tl*Sec. The left panel shows a surface representation of the complex (front view) showing the distribution of hydrophobic (yellow) and hydrophilic (cyan) amino acids. In the right panel, phosphatidylcholine lipid molecules modelled into the cryo-EM densities were additionally shown in a space-filling representation. **b**, A comparison of the Sec61 atomic models of ΔSec62 *Tl*Sec (in color) and WT *Tl*Sec [Sec62+/plug-closed] (in grey). Movements of TM2 (purple) and TM3 (violet) are indicated. **c**. As in Fig. 4a, but the WT *Sc*Sec structure by Wu et al. (EMDB-0440; ref. 29). Densities in cyan are detergent/lipid-like features. **f**, As in b, but comparing the structure by Wu et al. (in color; PDB 6ND1; ref. 29) and the *Sc*Sec[Sec62−] structure of the present study (in grey).
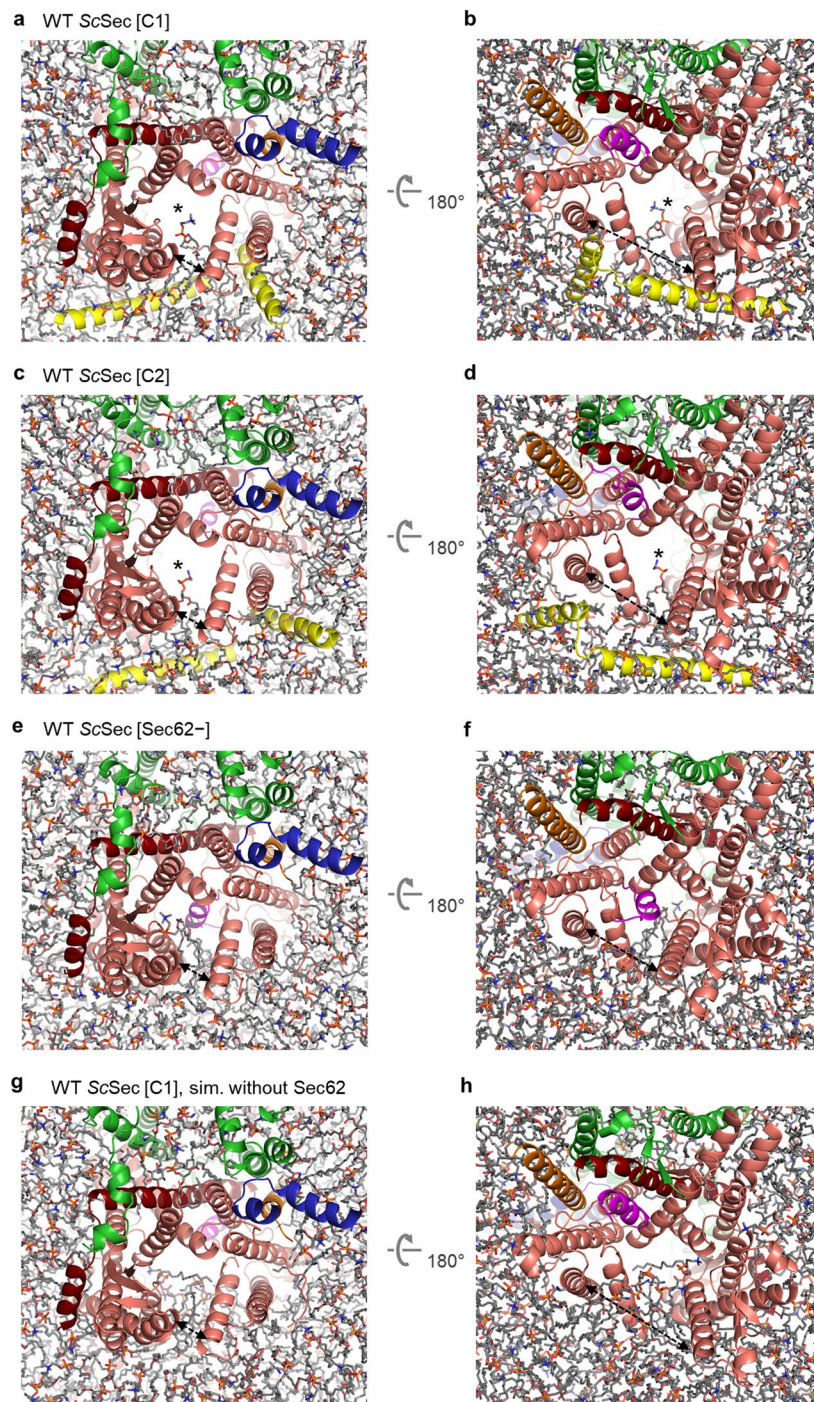
Extended Data Fig. 9 | All-atom MD simulations of the *Sc*Sec complex in a model lipid bilayer. a–h, As in Fig. 4 c–h, but with indicated *Sc*Sec structures. Panels a, c, e, and g are views from the cytosol, and b, d, f, and h are views from the ER lumen. In panels a–d, the translocation pore is marked by an asterisk. The lateral gate openings are indicated by a dashed arrow. The frames are from 200 ns after the initiation of the simulations.

Extended Data Fig. 10 | Structure of a fully closed *Sc*Sec complex containing FN3mut/Δ210-216 Sec63. a, Purification of the FN3mut/Δ210-216 *Sc*Sec complex. Left, a chromatogram from Superose 6 size-exclusion chromatography of the affinity purified mutant *Sc*Sec complex. Right, Coomassie-stained SDS-PAGE gel of the Superose 6 peak fraction. In this gel, Sec61γ (~10 kDa) migrated off the bottom. **b**, A representative cryo-EM micrograph. Scale bar, 50 nm. **c**, Examples of selected 2D class averages. **d**, A diagram of the cryo-EM single particle analysis procedure. **e**–**h**, The cryo-EM map (e and g) and atomic model (f and h). The color scheme is the same as in Fig. 1 a,d. The plug domain is shown in magenta. Shown are front (e and f) and side (g and h) views. An uncropped image for panel a is available as source data.

Corresponding author(s):   Eunyong Park

Last updated by author(s):   Oct 31, 2020

Reporting Summary

Nature Research wishes to improve the reproducibility of the work that we publish. This form provides structure for consistency and transparency in reporting. For further information on Nature Research policies, see our Editorial Policies and the Editorial Policy Checklist.

Statistics

For all statistical analyses, confirm that the following items are present in the figure legend, table legend, main text, or Methods section.

n/a	Confirmed	
☐	☒	The exact sample size (n) for each experimental group/condition, given as a discrete number and unit of measurement
☐	☒	A statement on whether measurements were taken from distinct samples or whether the same sample was measured repeatedly
☒	☐	The statistical test(s) used AND whether they are one- or two-sided *Only common tests should be described solely by name; describe more complex techniques in the Methods section.*
☒	☐	A description of all covariates tested
☒	☐	A description of any assumptions or corrections, such as tests of normality and adjustment for multiple comparisons
☒	☐	A full description of the statistical parameters including central tendency (e.g. means) or other basic estimates (e.g. regression coefficient) AND variation (e.g. standard deviation) or associated estimates of uncertainty (e.g. confidence intervals)
☒	☐	For null hypothesis testing, the test statistic (e.g. F, t, r) with confidence intervals, effect sizes, degrees of freedom and P value noted *Give P values as exact values whenever suitable.*
☒	☐	For Bayesian analysis, information on the choice of priors and Markov chain Monte Carlo settings
☒	☐	For hierarchical and complex designs, identification of the appropriate level for tests and full reporting of outcomes
☒	☐	Estimates of effect sizes (e.g. Cohen's d, Pearson's r), indicating how they were calculated

Our web collection on statistics for biologists contains articles on many of the points above.

Software and code

Policy information about availability of computer code

Data collection	For cryo-EM collection: Serial EM, For MD simulation: NAMD
Data analysis	Warp, cryoSPARC v2, PHENIX, Coot, Chimera, ChimeraX, PyMOL, Molprobity, VMD

For manuscripts utilizing custom algorithms or software that are central to the research but not yet described in published literature, software must be made available to editors and reviewers. We strongly encourage code deposition in a community repository (e.g. GitHub). See the Nature Research guidelines for submitting code & software for further information.

Data

Policy information about availability of data

All manuscripts must include a data availability statement. This statement should provide the following information, where applicable:
- Accession codes, unique identifiers, or web links for publicly available datasets
- A list of figures that have associated raw data
- A description of any restrictions on data availability

The atomic coordinates and cryo-EM density maps of the Sec complexes were deposited to the Protein Data Bank (PDB) and Electron Microscopy Data Bank (EMDB), respectively. Their PDB and EMDB accession codes are as follows: EMD-22785 for ScSec[consensus]; 7KAH and EMD-22770 for ScSec[Sec62−]; 7KAI and EMD-22771 for ScSec[C1]; 7KAJ and EMD22772 for ScSec[C2]; 7KAO and EMD-22778 for PM ScSec[Sec62−]; 7KAP and EMD-22779 for PM ScSec[C1]; 7KAQ and EMD-22780 for PM ScSec[C2]; 7KAR and EMD-22781 for FN3mut ScSec[Sec62−]; 7KAS and EMD-22782 for FN3mut ScSec[Sec62+]; 7KAT and EMD-22783 for PM/FN3mut ScSec[Sec62−]; 7KAU and EMD-22784 for PM/FN3mut ScSec[Sec62+]; 7KB5 and EMD-22787 for FN3mut/Δ210-216 ScSec; EMD-22786 for WT TlSec[Sec62+]; 7KAK and EMD-22773 for TlSec[Sec62−]; 7KAL and EMD-22774 for TlSec[Sec62+/plug-open]; 7KAM and EMD-22775 for TlSec[Sec62+/plug-closed]; 7KAN and EMD-22776 for ΔSec62 TlSec; EMD-22777 for Δanchor TlSec.

Field-specific reporting

Please select the one below that is the best fit for your research. If you are not sure, read the appropriate sections before making your selection.

☒ Life sciences ☐ Behavioural & social sciences ☐ Ecological, evolutionary & environmental sciences

For a reference copy of the document with all sections, see nature.com/documents/nr-reporting-summary-flat.pdf

Life sciences study design

All studies must disclose on these points even when the disclosure is negative.

Sample size	Sample sizes were not predetermined. For cryo-EM data, the samples were limited by available microscope time. Data was collected until we were able to refine a high enough resolution three dimensional reconstruction map to build an accurate model within the confines and limited microscope time. Yeast growth assays followed standard practices in the field. Assays contained millions of cells and we are only looking at the growth of the population of a specific yeast strain.
Data exclusions	No data was systematically excluded. The process of generating 3D maps from cryo-EM particles involves sorting for particles that are damages, have weak signal, or that are unlikely to refine correctly. This was implemented in Warp and cryoSPARC, and is standard practice in the field.
Replication	There was no attempt to replicate cryo-EM and MD simulation results. All biochemical experiments (yeast growth tests, SEC) have been replicated.
Randomization	Randomization was not attempted or necessary in this study.
Blinding	Blinding was not attempted or needed.

Reporting for specific materials, systems and methods

We require information from authors about some types of materials, experimental systems and methods used in many studies. Here, indicate whether each material, system or method listed is relevant to your study. If you are not sure if a list item applies to your research, read the appropriate section before selecting a response.

Materials & experimental systems

n/a	Involved in the study
☒ ☐	Antibodies
☐ ☒	Eukaryotic cell lines
☒ ☐	Palaeontology and archaeology
☒ ☐	Animals and other organisms
☒ ☐	Human research participants
☒ ☐	Clinical data
☒ ☐	Dual use research of concern

Methods

n/a	Involved in the study
☒ ☐	ChIP-seq
☒ ☐	Flow cytometry
☒ ☐	MRI-based neuroimaging

Eukaryotic cell lines

Policy information about cell lines

Cell line source(s)	Common yeast strains (BY4741, yMLT62) were requested/gifted from labs per standard practice or obtained commercially (Hughes collection TH_4087, TH_5187; Dharmacon).
Authentication	Not applicable.
Mycoplasma contamination	Not applicable.
Commonly misidentified lines (See ICLAC register)	No commonly misidentified cell lines were used.